ICE THICKNESS ESTIMATION USING LOW FREQUENCIES, AND AN INVESTIGATION OF DIFFRACTION OF SOUND IN SAMPLES WITH MICRO STRUCTURES USING ULTRASOUND

A Thesis
Presented to
The Academic Faculty

by

Anurupa Shaw

In Partial Fulfillment
of the Requirements for the Degree
Master in Science in the
George W. Woodruff School of Mechanical Engineering

Georgia Institute of Technology
May 2014

ICE THICKNESS ESTIMATION USING LOW FREQUENCIES, AND AN INVESTIGATION OF DIFFRACTION OF SOUND IN SAMPLES WITH MICRO STRUCTURES USING ULTRASOUND

Approved by:

Dr. Nico F. Declercq, Advisor
School of Mechanical Engineering
Georgia Institute of Technology

Dr. Massimo Ruzzene
School of Aerospace Engineering
Georgia Institute of Technology

Dr. Badreddine Assouar
Institut Jean Lamour
Université de Lorraine, France

Date Approved: 25/03/2014

ACKNOWLEDGEMENTS

First and foremost I offer my sincerest gratitude to my supervisor, Dr. Nico F. Declercq, who has guided and supported me throughout my stay in France with his patience and knowledge whilst allowing me the room to work in my own way. I attribute the level of my Masters degree to his encouragement and effort. Without his motivation this thesis would not have been possible. He has always shown faith in me. One simply could not wish for a better or friendlier supervisor.

I would like to thank my committee members Dr, Nico F. Declercq, Dr. Massimo Ruzzene and Dr. Badreddine Assouar, for their valuable comments and suggestions that helped me improve my work documented in this thesis.

I feel blessed to be a part of a prudent, talented, knowledgeable and supportive group of research students. Rayisa Moiseyenko, Peter McKeon, Jigfei Liu and Qi Wang have always been there for me, helping me with experiments and difficult concepts in Acoustics. I admire them for the kindness and generosity they have shown me. I would like to express my gratitude to them for everything they have done for me. I hold my advisor and team members responsible for all the positive changes in me as a researcher and as a person that I have become over the years of my stay in France. They are like a second family to me.

I would also like to thank Prof. Suk Wang Yoon, for his input and guidance. The staff at Georgia Tech Lorraine and Georgia Tech Atlanta has been very helpful and considerate throughout. I cannot thank them enough for helping me with all the paperwork required not just for my thesis, but also my stay in France. I would like to

thank Isabelle Hindre for her optimism and support during my entire stay in France and for being a wonderful friend. I am very happy to have known such a wonderful person.

Lastly, I would like to thank my parents, my sister and my friends, for having faith in me and always motivating me to do what is right. If it had not been for my sister, I would have never been able to go this far. Thank you all for being there for me.

TABLE OF CONTENTS

	Page
ACKNOWLEDGEMENTS	iii
LIST OF TABLES	vii
LIST OF FIGURES	viii
SUMMARY	x
1 INTRODUCTION	1
1.1 Previous work on ice thickness determination	1
1.2 Properties of ice	4
1.3 Brief history of acoustic microscopy	4
1.4 Background study of diffraction of sound	5
2 DETERMINATION OF ICE THICKNESS USING AUDIO SOUND	7
2.1 Analytical model	7
2.1.1 Simulation of a knock	10
2.1.2 Boundary conditions	13
2.2 Discussion of the simulated results	14
2.3 Experiment	18
2.4 Analysis of the recorded audio signal	19
2.5 Appearance of an echo	21
2.6 Comparison of simulated and experimental results	23
2.7 Musical note for every thickness of thin layers of ice	26
3 INVESTIGATION OF SOUND DIFFRACTION BY PERIODIC STRUCTURES USING ACOUSTIC MICROSCOPY	28
3.1 Motivation	28

3.2 Description of the technique 29
3.3 Experiments and discussion 31
3.3.1 Brass periodic Structures 31
3.3.1.1 Hill height estimation 32
3.3.1.2 Reliability check 37
3.3.1.3 Error estimation 40
3.3.1.4 Diffraction of sound 41
3.3.2 Periodic structures on Sapphire 42
3.3.2.1 Hill height estimation 43
3.3.2.2 Reliability check 48
3.3.2.3 Diffraction of sound 49
4 CONCLUSION AND FUTURE WORK 51
APPENDIX A: Stress and displacement equations for elastic waves in ice 54
APPENDIX B: THE SCANNING ACOUSTIC MICROSCOPE 58
B.1 Working of the Scanning Acoustic Microscope 58
B.1.1 User interface 59
B.1.2 Acoustic Lens 61
B.1.3 Software setting optimization 63
B.1.4 Image acquisition and data storage 64
B.1.5 V (z) curve generation 65
B.1.6 Limitations of the scanning acoustic microscope 67
REFERENCES 69

LIST OF TABLES

Page

Table 1: General rules for maximum load for different thicknesses of ice. 3

Table 2: Comparison of experimental results and simulated results of (f x d) in [Hz. m] of the plate mode described above. 25

Table 3: Comparison of the calculated hill height for case 1 (different positions on the valley) and case 2 (different positions on the plane surface). 35

Table 4: A comparison between the hill heights and hill widths respectively, obtained from an acoustic image and optical image. 36

Table 5: Estimation of the longitudinal velocity, shear velocity and the shear modulus for different transducers. 39

Table 6: Comparison of the calculated hill height for case 1 (different positions on the hill) and case 2 (different positions on the plane surface). 46

Table 7: A comparison between the hill heights and periodicities respectively, obtained from an acoustic image and optical image. 47

Table 8: Specification of the setup and calculated results for the Sapphire sample. 48

Table 9: A comparison of the estimated longitudinal velocity, shear velocity and the shear modulus with the known values. 48

Table 10: The different parts of the scanning acoustic microscope. 58

Table 11: Name and description of the different parts of the user interface. 60

LIST OF FIGURES

Page

Figure 1: Schematic representation of the analytical model developed using plane wave theory described in the above section. 8

Figure 2: Representation of the transmission coefficients for an ice plate of 39 mm thickness for a frequency range of 0 MHz - 0.15 MHz. 14

Figure 3: Schematic representation of the analytical model after the adjustment is made in order to incorporate the effect in the acoustic emission due to reflection from the bottom surface of the lake. 16

Figure 4: Representation of the reflection coefficients (for case 3) for an ice plate of 39 mm thickness for a frequency range of 0 MHz - 0.15 MHz. 16

Figure 5: Representation of the reflection coefficients (for case 3) for an ice plate of 39 mm thickness for a frequency range of 0 Hz-20 kHz. It is a zoomed representation of Fig. 4 for a narrower frequency range. 17

Figure 6: Experimental setup. The height range is 0.5 m - 1.5 m. The width of the 'Lac Symphonie' is calculated to be 66.5 m (± 2 m). 18

Figure 7: Spectrogram of a pulse recorded at a height of 1.00 m from the ice plate for 39 mm thickness of ice showing the frequencies with high amplitudes in the audio spectrum of the recorded signal for one pulse (i.e. a knock). 19

Figure 8: A zoomed representation of Figure 7 which shows the low frequencies showing high amplitudes for a long period of time. 20

Figure 9: Spectrogram of a pulse recorded at a height of 1m from the ice plate thickness of 28.5 mm, (for 'lac Symphonie') showing the frequencies with high amplitudes in the audio spectrum of the recorded signal for one pulse (i.e. a knock). 22

Figure 10: Representation of the reflection coefficients for an ice layer (39 mm in thickness) with air on top and water below for a frequency range 20 Hz - 20 kHz and phase velocity range (0 - 2000 m/s).It is a zoomed representation of Figure 5. 23

Figure 11: The curve representing the relation between the frequency and the thicknesses of ice. 26

Figure 12: A chart to assign a musical note (key frequencies of a piano) to the thicknesses. 27

Figure 13: (a) Schematic representation of the Scanning Acoustic Microscope. 30
(b) Diagrammatic representation of the wave model of an acoustic lens showing the focusing effect. 30

Figure 14: (a) Image of the brass sample taken by a camera,
(b) Image obtained using an optical microscope,
(c) Diagrammatic representation of a section of the sample and
(d) Image obtained using SAM. Transducer frequency used is 400 MHz. 32

Figure 15: V (z) curve for the brass sample. Transducer frequency used is 400 MHz. 33

Figure 16: Side view of the sample obtained using an optical microscope. 34

Figure 17: FFT of the V (z) curves. Transducer frequency used is 400 MHz. 38

Figure 18: A plot of the difference between the FFT curves in figure 17. 39

Figure 19: (a) An acoustic image of the corrugated area.
(b) A small section of the corrugated region selected from the image 19 (a). 42

Figure 20: An optical image of the corrugated region on the sample surface obtained using an optical microscope. 42

Figure 21: V (z) curves for the periodic structures on Sapphire. The transducer frequency used is 1.09 GHz. 43

Figure 22: V (z) curves for the periodic structures on Sapphire. The transducer frequency used is 1.09 GHz. 45

Figure 23: The scanning acoustic microscope (SAM 2000). 58

Figure 24: The user interface for the scanning acoustic microscope. 59

Figure 25: (a) A focused transducer with a frequency range of 0.8 – 1.3 GHz.
(b) A 400 MHz focused transducer. 62

Figure 26: The settings panel for controlling the automated V (z) scan. 66

SUMMARY

First, the thickness of ice on lakes and canals is estimated by analyzing the sound spectrum generated by dispersion of Lamb type waves propagating in ice. In winters when lakes and canals freeze, it is important to know the thickness of the ice layer before setting foot on it. When a stone is thrown on the ice layer, acoustic waves are generated and a fluting sound can be heard. This is recorded for different thicknesses of ice, and the sound spectrum is compared with the results simulated using a parameterized model. This numerical model is created using a combination of plane waves for different incident angles and frequencies to generate dispersion curves for different thicknesses of ice. The frequencies of the reflected sound are then compared with the frequencies of musical instruments in order to assign different musical notes to different thicknesses of ice. The technique enables thickness estimation without the use of specialized equipment or time consuming drilling and may therefore be of practical value in the preservation of the lives of ice skaters and playing children.

Second, a scanning acoustic microscope with high ultrasonic frequencies is used to investigate samples with micro structures. Acoustic microscopy is a well known technique. V (z) curves have been used earlier by several researchers to investigate the visco-elastic parameters of thin samples like composites, animal tissue, etc. In this work however, this technique is used to characterize corrugation on thin samples with different periodicities and to investigate diffraction of sound by periodic structures of high periodicity, for high frequencies.

CHAPTER 1

INTRODUCTION

Walking on ice, skating on ice, ice fishing (with or without a car), sledding, cross-country skiing, snowmobiling, and playing different kinds of sports on ice can be dangerous activities if one is unable to determine correctly whether the ice is thick enough to withstand the weight. There are several ways to estimate the potential safety of ice, such as measuring its thickness and observing its color .External factors such as temperature, snow and local conditions should also be kept in mind. Direct methods[1] generally involve ultrasound, radar or drilling equipments for measuring the thickness which are obviously either expensive, time consuming or simply not available at the time of need. Ice can be very complicated in structural composition and geometry. However here we focus on a simple case of ice on lakes or canals which is normally as good as isotropic and as uniform in thickness as can be. This situation is particularly of highest interest to most situations in which skaters or playing children are tempted to enjoy a winter day on frozen lakes, ponds, canals and perhaps even slowly flowing rivers.

1.1 Previous work on ice thickness determination

To sketch a more general framework of ice thickness determination, some indirect methods have been suggested for measuring Arctic ice thickness by researchers over the years[2]. Use of observed ice motion and wind data has been suggested by Lewis[3] and Crissman[4] .As wind blows over an ice floe, the energy of the wind is transferred through the ice which causes the ice layer to move[4]. Another interesting suggested approach is measurement of ice thickness using observed noises created by crack propagation in the ice. Thermal tension and effects of the wind and water current beneath cause mechanical

and thermal stress within the ice leading to its rupture[3]. Both these methods though work well in ice thickness estimation, are time consuming, cannot be executed by people without specialized equipment wanting to cross a lake and one requires a prior knowledge of acoustics to use them.

This work is intended to provide a method that is much more practical and can be used as an easy tool to estimate the thickness of ice by common people. When one knocks on ice, surface waves are generated, a part of which is reflected, i.e. re-emitted into the atmosphere. The acoustic emissions perceived by the human ear as a fluting noise, are analysed to determine a relationship between the reflected sound and the thickness of ice. In other words, we use low frequencies, i.e., the audible range (20 Hz-20 kHz), to estimate the thickness of ice.

In the past, Ewing and Crary[5-7] had studied propagation of air coupled flexural waves in ice. A thickness vs. frequency relationship had been derived as a ratio earlier. This ratio depends on different parameters of the lake and is different for different lakes. In order to obtain this relationship, geophones and seismometers have been used to record the experimental data. However if one is not aware of this ratio for a particular lake, one cannot use this relationship for a good estimation of the thickness. The method suggested in this work is more general and can be used for different lakes and canals. Experimental data from different lakes have been used to verify the analytical solution.

Several other researchers[5-33] had focused primarily on developing dispersion curves for ice plates to investigate dispersion effects or change in group velocity, etc., where ice thickness estimation was an application for thick layers of ice. The readers need to keep in mind that the previous studies had been done for thick layers of ice (i.e.

1.10 ft thick) and for higher frequency ranges (not the audible range). This fluting noise is distinct for thin layers of ice. It was not taken into account by Ewing and Crary[5-7], possibly because they dealt with large thicknesses and the frequency of the fluting was too low and arrived too late. For thicknesses we consider, the fluting is distinct and is practical to use because this is what an ice skater or people who intend to walk on ice, can hear. If they can use the fluting noise to determine the thickness of ice, they would not require seismographs, geophones and other heavy equipments.

In general, rules for ice thickness and corresponding maximum load exist[15]. A summary is given in Table 1.

Table 1: General rules for maximum load for different thicknesses of ice.

THICKNESS OF ICE	**BEST SUITED FOR**
3" (7 cm) (new ice)	KEEP OFF
4" (10 cm)	suitable for ice fishing, cross-country skiing and walking (approx. 90 kg)
5" (12 cm)	suitable for a single snowmobile or ATV (approx. 360 kg)
8" - 12" (20 cm - 30 cm)	suitable for one car, group of people (approx. 680 kg - 900 kg)
12" - 15" (30 cm - 38 cm)	suitable for a light pickup truck or a van

1.2 Properties of ice

Ice in itself can be very complex. Ice can assume a large number of different crystalline structures, more than any other known material. At ordinary pressures the stable phase of ice is called "ice I", and the various high-pressure phases of ice number up to "ice XIV" so far[16]. Ice formation involves complex physical processes that are difficult to observe in most cases because they occur out of view beneath the surface[17]. Ice can be modelled in several ways but due to its complex crystalline structure, it is very difficult to incorporate and simulate all the possible variables and all the thermodynamic processes. For simplicity of the problem in this work, the ice layer is considered to be a homogeneous isotropic plate. This simplification is justified for the case of ice on lakes, ponds and canals and, as will be seen further on in this work, results are in good agreement with the experiments.

1.3 Brief history of acoustic microscopy

Acoustic microscopy has proved to be an attractive tool to study composites, rocks, biological matrix. The scanning acoustic microscope (SAM) is known to be very effective for studying pores, bonding of material layers, cracks and other kinds of defects in a sample without destroying the sample itself. It also has several applications in the field of biomedical engineering. Researchers have developed several techniques using SAM to study micro-structures like crystals and animal tissue. They have analyzed several aspects of such samples, like the stresses developed in them with time, and have explored the dynamics of physiochemical processes taking place in them[34-52].

The first scanning acoustic microscope was developed by Lemon and Quate[36] in 1974. They used a through-transmission approach to make C-scans. An acoustic image in

the shape of a grating was produced by a focused ultrasonic beam that scanned a 200-mesh copper electron microscope grid. In a through-transmission technique, one transducer is used to send a signal while another one is used to receive it. The SAM used in the work described here, however, uses the reflection technique, whereby a single transducer sends and receives the signal. This circumvents the problem of aligning two transducers.

The scope for applications of acoustic microscopy is huge and is growing rapidly. In the past few decades, there have been reports about application of acoustic microscopy in the study of steel integrated structures, in ferro-elastic ceramics, study of human retina, semiconductors, silicon nitride composites, etc. In this work, an attempt is made to explore yet another possible application, which is diffraction of sound using high frequencies.

1.4 Diffraction of sound

Diffraction is a change in direction of waves as they pass through an opening or around an obstacle in their path. As the wavelength increases, the amount of diffraction (the sharpness of the bending) increases[42]. If the wavelength of the wave is smaller than the obstacle or opening, no noticeable diffraction occurs. The attenuation is very high for high frequencies.

When sound is diffracted by periodic structures, interesting effects are noticed in the reflection and transmission spectra. These effects have been used to describe different phenomena like Wood anomalies first described by Wood, or leaky Scholte-Stoneley waves propagating backward described by Declercq et al. Herbison, Declercq and Liu have used a study of Wood anomalies and other diffraction effects to characterize

(estimate the geometric parameters) periodic surfaces for low frequencies[42-47]. In this work, high frequency (400 MHz – 1.09 GHz) focused transducers are used to characterize the corrugation on samples with different periodicities. Also, samples with periodic structures with high periodicity (1- 4 μm) are investigated for diffraction effects.

CHAPTER 2

DETERMINATION OF ICE THICKNESS USING AUDIO SOUND

2.1 Analytical Model

In this method, the ice layer is considered to be an isotropic plate embedded in water with air on top. For the simplicity of the problem the plate is considered to be thin, smooth and of uniform thickness. Alternatively, a thick plate model would include effects of rotary inertia along with transverse shear. Past work of Fox and Squire[11-12] show that a thick plate model is unnecessary except in the case of very thick plates or very high frequencies.

When one knocks on the ice, Lamb type waves are generated in the plate; this causes acoustic emissions in air which comprise of primary reflections and re-emissions from the plate. A parameterized model is developed based on plane wave theory. Plane waves of different frequencies incident at different angles are used to obtain dispersion curves for a given thickness.

For plates, water-loaded on both sides, a pair of largely fluid-borne waves consisting of a symmetric(S) and anti-symmetric (A) mode exist, along with leaky (or pseudo) Lamb wave modes very similar to the free-plate Lamb waves. If the water loading is removed from one side of the plate, the symmetric mode disappears and only the anti-symmetric mode remains. This remaining mode is the one that has been referred to as the 'Scholte-Stoneley wave' by e.g. Sessarego[18]. In the current study, the ice plate is loaded with water on one side and air on the other. The density of ice (900 kg/m^3 is close to that of water (1000 kg/m^3) whereas the air density is very low (0.23 kg/m^3), this causes a high acoustic impedance difference at the air-ice interface. The plate is heavily loaded

on the other side, i.e. at the ice-water interface the impedance difference is comparatively lower. This gives rise to more complexities unlike the case of a steel plate loaded with water on one side and air on the other, where the impedance difference between steel and water is very high.

As a matter of fact when a solid plate is in air, a knock generates Lamb waves. It has been observed that the cut-off frequencies for the Lamb modes correspond to the resonance frequencies of the plate[19]. However the case studied here is very different, i.e. ice loaded with water at one end and having properties close to water. Here the acoustic emission is mainly due to re-emissions from the ice after reflection from the bottom surface of the lake. In addition, in the audio range no cut-off frequencies for Lamb modes have been observed, neither in the simulations nor the experimental results. Here, in the case of ice covering water and covered by air, the observed phenomenon is due to an observed plate mode referred to as 'Scholte wave mode' by e.g. Destrade[20]. This mode is dispersive in the audible range.

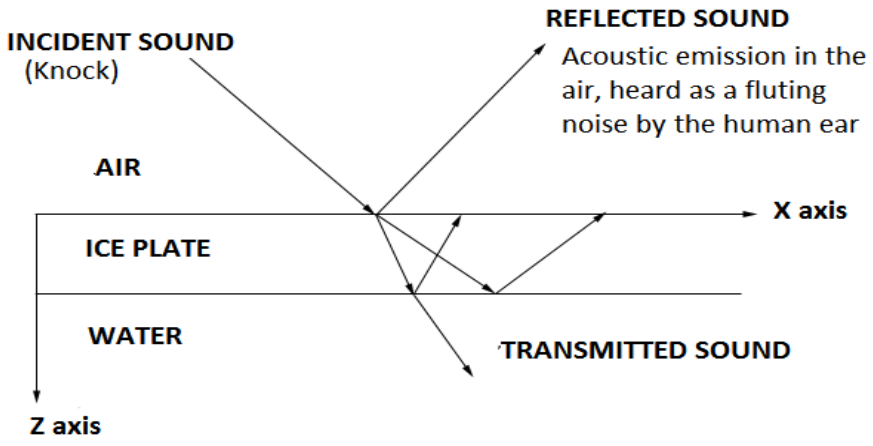

Figure 1: Schematic representation of the analytical model developed using plane wave theory described in the above section.

This plate mode is anti-symmetric in nature. To account for the wave propagation in this isotropic plate of ice shown in Figure 1, the equations of motion and stress-strain relations taken into account are:

$$\boldsymbol{\sigma_{ij} = \lambda \varepsilon_{kk} \delta_{ij} + 2\mu \varepsilon_{ij}} \quad (1)$$

where λ and μ are the two Lame's constants of the material. The strain- displacement relations are:

$$\boldsymbol{\varepsilon_{ij}} = \frac{\mathbf{1}}{\mathbf{2}} [\bar{u}_{i,j} + \bar{u}_{j,i}] \quad (2)$$

Using Helmholtz's representation the displacement ū in an isotropic material can be written in terms of a scalar potential ϕ and a vector potential ψ where:

$$\bar{u} = \mathbf{grad}\ \phi + \mathbf{rot}\ \boldsymbol{\psi} \quad (3)$$

where

$$\mathbf{div}\ \boldsymbol{\psi} = \mathbf{0} \quad (4)$$

with the scalar potential and the vector potential satisfying the respective conditions:

$$\boldsymbol{\nabla^2 \phi} = \frac{\mathbf{1}}{\mathbf{v_l^2}} \frac{\partial^2 \phi}{\partial t^2} \quad (5) \ , \quad \mathbf{v_l^2} = \frac{\boldsymbol{\lambda + 2\mu}}{\boldsymbol{\rho}} \quad (6)$$

$$\boldsymbol{\nabla^2 \psi} = \frac{\mathbf{1}}{\mathbf{v_s^2}} \frac{\partial^2 \bar{\psi}}{\partial t^2} \quad (7) \ , \quad \mathbf{v_s^2} = \frac{\boldsymbol{\mu}}{\boldsymbol{\rho}} \quad (8)$$

where v_l and v_s are longitudinal velocity and shear wave velocity respectively.

with the $\boldsymbol{\nabla}^2$ given by:

$$\boldsymbol{\nabla^2} = \frac{\partial^2}{\partial x^2} + \frac{\partial^2}{\partial y^2} + \frac{\partial^2}{\partial z^2} \quad (9)$$

The decomposition of the displacement vector generally simplifies the solution of a boundary value problem.

2.1.1 Simulation of a Knock

Simulating a "knock" on ice can be achieved using different types of forced boundary conditions. This "knock" or in other words the incident wave is represented by a summation of plane waves propagating at different angles with different frequencies. This incident wave is converted into several modes which propagate in and around the object contributing to the scattered field. For the presented model each plane wave is considered incident on an air/solid interface, a part of which is reflected in air and another part of it refracted in the ice plate which accounts for the longitudinal and shear waves in the plate. Due to the linearity of the problem, the low amplitudes that are hereby transmitted into the ice layer can be increased by multiplication by any desired factor. If in reality nonlinearities appear due to local breaking of the ice for instance, higher harmonics can presumably exist, but this is ignored in our model, one reason being that the human ear is assumed to distinguish between the louder first harmonics and the quieter higher harmonics. Additionally it is known that damping also increases for higher frequencies. At the bottom of the plate i.e. the solid/water interface, a longitudinal wave is transmitted. A coordinate system is used such that the interfaces are normal to the z-axis and the waves propagate in the x-z plane.

A harmonic plane wave is represented by:

$$\bar{u} = \mathbf{A}e^{\mathbf{i}[\,\mathbf{k}\bar{r}.\bar{e}_{\mathbf{k}}-\omega\mathbf{t}]}\,.\,\bar{\mathbf{e}}_{\mathbf{p}} \quad (10)$$

where:

A is the complex amplitude,

k is the wave number related to the wavelength λ by $k = 2\pi/\lambda$ and angular frequency ω,

e_p is the unit polarization vector defining the direction of particle motion

From Snell's law it is known that the x-component of the wave vectors of all the waves that appear in this system are equal hence are replaced by the x component of the incident wave vector and that the time dependence of all these waves is simple harmonic ($e^{-i\omega t}$)[21-22]. Since all velocity potentials contain the common factor exp [i(k_x x -ωt)] , it is omitted from the calculations.

The wave potentials for each medium can be written as:

$$\phi_1 = [\mathbf{P}e^{\mathbf{i(z-z_s)K_{z,1}}} + \mathbf{Q}e^{\mathbf{-i(z-0)K_{z,1}}}] \quad (11)$$

$$\phi_2 = [\mathbf{A}e^{\mathbf{i(z-0)K_{z,2}}} + \mathbf{B}e^{\mathbf{-i(z-z_a)K_{z,2}}}] \quad (12)$$

$$\psi_2 = [\mathbf{C}e^{\mathbf{i(z-0)L_{z,2}}} + \mathbf{D}e^{\mathbf{-i(z-z_a)L_{z,2}}}] \quad (13)$$

$$\phi_3 = [\mathbf{F}e^{\mathbf{i(z-z_a)K_{z,3}}}] \quad (14)$$

Where:

z_s represents the height of the source of the incident wave from the surface of the ice layer. In our model (z_s = 0).

z_a represents the thickness of the ice layer.

1, 2, 3 suffixes represent the three mediums air, ice and water respectively. **K** and **L** are z-components of the wave vectors of longitudinal and shear waves respectively:

$$\mathbf{K} = \sqrt{(\omega/\mathbf{v_d})^2 - \mathbf{k_x^2}} \quad (15)$$

$$\mathbf{L} = \sqrt{(\omega/\mathbf{v_s})^2 - \mathbf{k_x^2}} \quad (16)$$

The displacement vectors are given by:

$$\bar{u}_x = \frac{\partial \phi}{\partial x} - \frac{\partial \psi}{\partial z} \quad (17)$$

$$\bar{u}_y = 0 \quad (18)$$

$$\bar{u}_z = \frac{\partial \phi}{\partial z} + \frac{\partial \psi}{\partial x} \quad (19)$$

Using the stress relations mentioned earlier the components of the stress tensor are calculated as:

$$T_{zz} = \lambda\left(\frac{\partial^2 \phi}{\partial x^2} + \frac{\partial^2 \phi}{\partial z^2}\right) + 2\mu\left(\frac{\partial^2 \phi}{\partial z^2} + \frac{\partial^2 \psi}{\partial x \partial z}\right) \quad (20)$$

$$T_{xz} = 2\mu\left(\frac{\partial^2 \phi}{\partial x \partial z} + \frac{1}{2}\left(\frac{\partial^2 \psi}{\partial x^2} - \frac{\partial^2 \psi}{\partial z^2}\right)\right) \quad (21)$$

For the medium 2 (ice), the stress and displacement relations are given by the above relations. Medium 1 (air) and medium 3 (water) are considered for the presented problem to be ideal elastic fluids hence the stress equations are reduced to:

$$T_{zz,m} = \lambda\left(\frac{\partial^2 \phi_m}{\partial x^2} + \frac{\partial^2 \phi_m}{\partial z^2}\right) + 2\mu\left(\frac{\partial^2 \phi_m}{\partial z^2}\right) \quad (22)$$

$$T_{xz,m} = 2\mu\left(\frac{\partial^2 \phi_m}{\partial x \partial z}\right) \quad (23)$$

and the displacement relations are reduced to:

$$\bar{u}_{x,m} = \frac{\partial \phi_m}{\partial x} \quad (24)$$

$$\bar{u}_{z,m} = \frac{\partial \phi_m}{\partial x} \quad (25)$$

where m=1 for medium 1 and m=3 for medium 3. The resultant expressions for formula (22-37) are given in the appendix.

2.1.2 Boundary conditions

The boundary conditions for continuity of normal stress and strain at the air/solid interface are given by:

$$\bar{u}_z^1 = \bar{u}_z^2 \qquad (38)$$

$$\mathbf{T}_{xz}^1 = \mathbf{T}_{xz}^2 = \mathbf{0} \qquad (39)$$

$$\mathbf{T}_{zz}^1 = \mathbf{T}_{zz}^2 \qquad (40)$$

and for the solid/water interface by:

$$\bar{u}_z^2 = \bar{u}_z^3 \qquad (41)$$

$$\mathbf{T}_{xz}^2 = \mathbf{T}_{xz}^3 = \mathbf{0} \qquad (42)$$

$$\mathbf{T}_{zz}^2 = \mathbf{T}_{zz}^3 \qquad (43)$$

Applying the boundary conditions and separating the known and unknown terms a linear system of six equations is obtained:

$$[\mathbf{A}]\{\mathbf{Y}\} = \{\mathbf{N}\} \qquad (44)$$

which is solved for $$\{\mathbf{Y}\} = \begin{bmatrix} \mathbf{Q} \\ \mathbf{A} \\ \mathbf{B} \\ \mathbf{C} \\ \mathbf{D} \\ \mathbf{F} \end{bmatrix} \qquad (45)$$

in which the amplitude coefficients appear for all the waves in the developed model.

This system of equations can be used to calculate the reflection and the transmission coefficients along with coefficients for the longitudinal and shear waves

within an isotropic plate. When these coefficients are plotted for the phase velocities corresponding to the whole range of incident angles and frequencies, exotic features (variation in amplitude of these coefficients for different frequency and phase velocity combinations) are obtained that correspond to the dispersion curves.

2.2 Discussion of the Simulated Results

As 'Case 1', the reflection coefficient is studied ignoring the possibility of sound being reflected back from the bottom of the lake after transmission through the ice. The reflection coefficients obtained from the simulation for this case do not show any interesting features.

As 'Case 2', the transmission coefficients of waves from ice into the underlying water are studied. The results are shown in Figure 2.

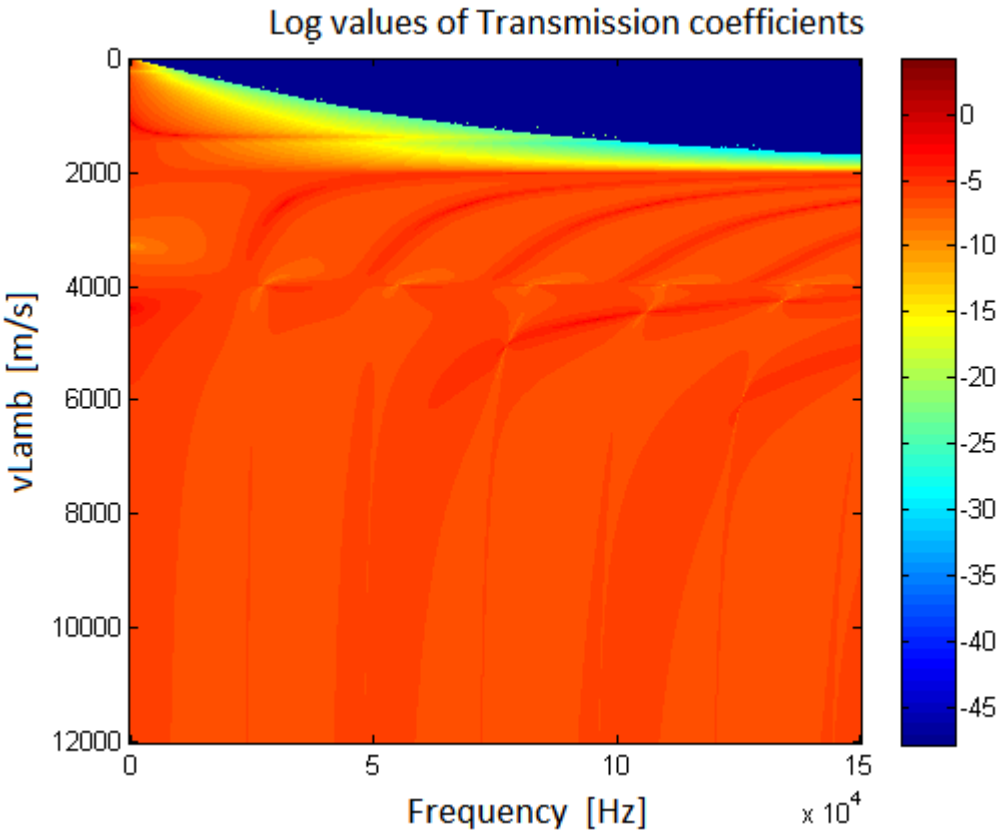

Figure2: Representation of the transmission coefficients for an ice plate of 39 mm thickness for a frequency range of 0 MHz - 0.15 MHz.

The transmission coefficients plotted with respect to frequency, for the same parameters in Figure 2 shows exotic features (i.e. variation in the amplitudes of the transmission coefficients for different phase velocities and frequencies, which describe plate modes).These correspond to dispersion curves of a 39 mm thickness of ice embedded in water with air on top. When these coefficients are plotted for (f x d) (i.e. frequency [Hz] x thickness of the plate [m]) in order to obtain dispersion curves, the features in the two plots are exactly equal except that in the latter case the image is rescaled.

As ‘Case 3’, perfect reflection from the bottom of the lake is assumed, instead of being ignored as in previous cases. As discussed earlier when a stone is thrown on a frozen lake a fluting sound can be clearly heard. Since the knock is on an ice layer of a lake, the distance between the ice layer and the bottom surface of the lake is not very large. Hence a part of the total acoustic emission in air is due to reflection from the ground below the ice layer. To incorporate this effect in the simulation, a reverse model of our problem is added to the initial simulation. The sound transmitted through the ice layer, in the water strikes the ground which is considered to be a perfect reflector for the simplicity of the problem. This sound is transmitted back from water through the ice layer into air and contributes to the fluting sound that can be heard.

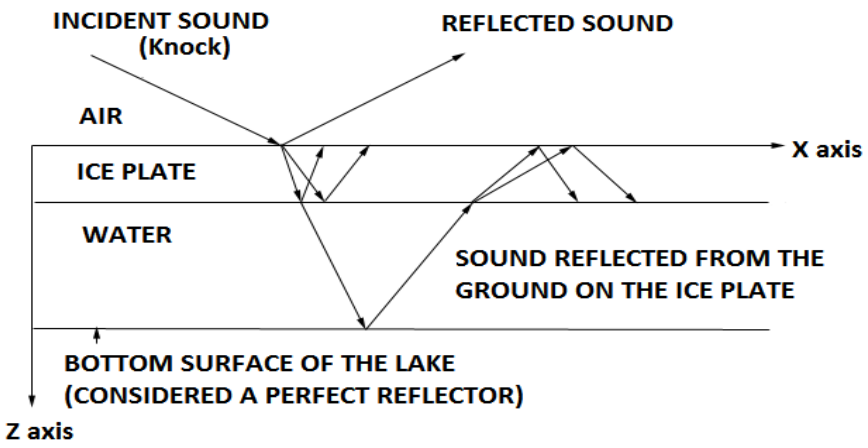

Figure 3: Schematic representation of the analytical model after the adjustment is made in order to incorporate the effect in the acoustic emission due to reflection from the bottom surface of the lake.

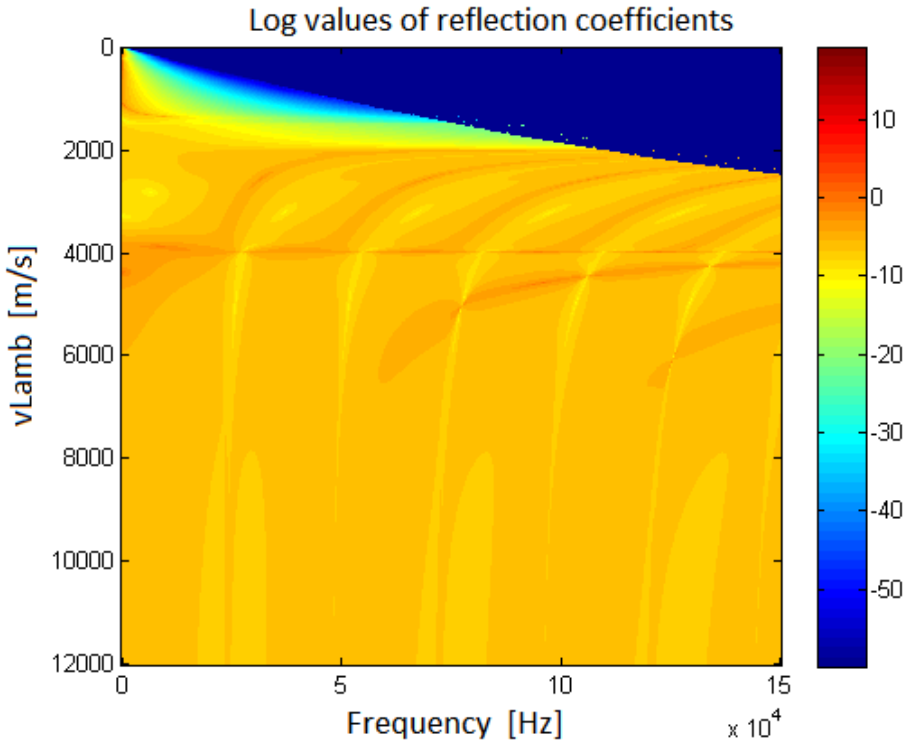

Figure 4: Representation of the reflection coefficients (for case 3) for an ice plate of 39 mm thickness for a frequency range of 0 MHz - 0.15 MHz.

Figure 3 depicts a representation of the analytical model for ‘case 3’ incorporating the effect of reflections from the bottom surface of the lake. In Figure 2 and 4 the plot represents the logarithmic values of the transmission coefficients and reflection coefficients for unit amplitude of incident sound. In a real case, the amplitude of a knock is multiple times higher. Though as indicated earlier, that does not alter the features of the plot; just the amplitude of the coefficients increase several folds by the same ratios. When we focus on the area of interest, i.e. if we are trying to determine the thickness of ice using audio sound, the dispersion curves are only of interest within the audible range i.e. 20 Hz - 20 kHz. The particular area is focused on in Figure 5.

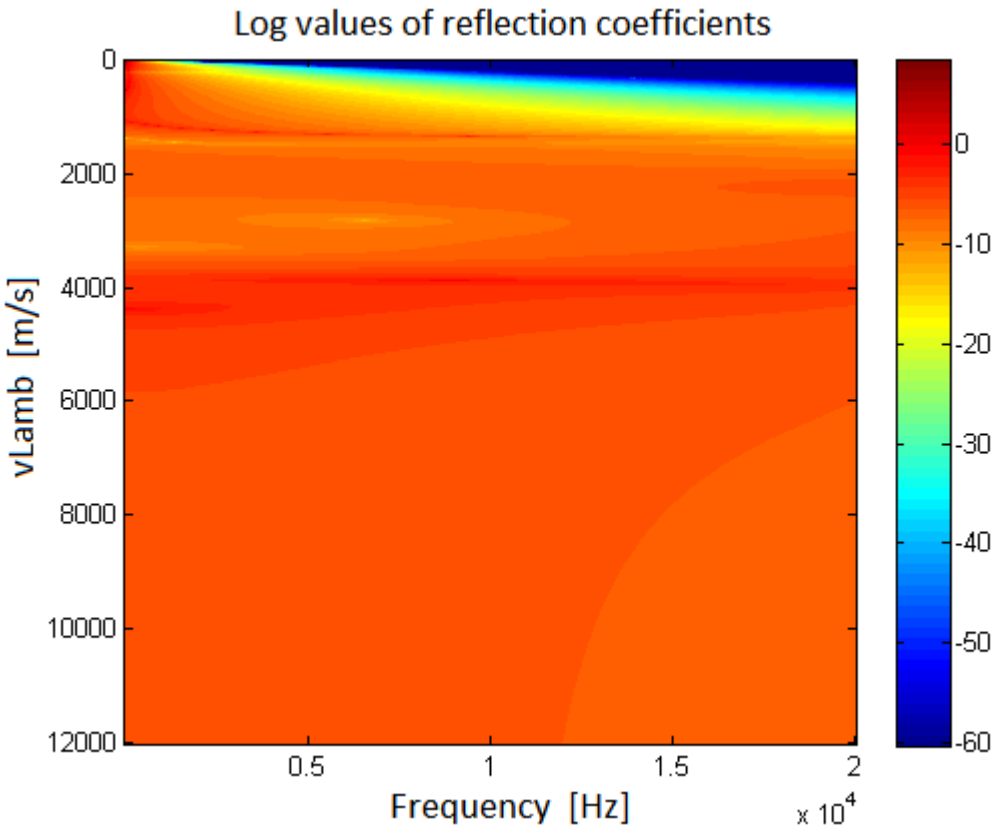

Figure 5: Representation of the reflection coefficients (for case 3) for an ice plate of 39 mm thickness for a frequency range of 0 Hz-20 kHz. It is a zoomed representation of Figure 4 for a narrower frequency range.

In the audible range, for thin layers of ice (thickness less than 0.30 m), a flexural mode with very low amplitude is observed in Figure 5, along with an additional plate mode with a velocity lower than the Rayleigh wave velocity. This additional plate mode cannot be called a Lamb mode or a pure flexural mode.

2.3 Experiment

Experiments have been done on a frozen lake (first at the lakes of 'Evolis Park' in Kortrijk, Belgium, later on 'Lac Symphonie' and nearby ponds in Metz, France). The reflected sound generated by several knocks on the ice, are recorded for each knock from different heights from the ice layer (0.10 m to 1.50 m) and for different thicknesses by a regular microphone. Right after each experiment, a hole is drilled to measure the thickness using a micrometer. The thickness is measured at different positions along the circumference of the hole. Measurements are taken for 19 mm and 42 mm thickness of ice on the lakes of 'Evolis Park' in Kortrijk, Belgium and for 28.5 mm, 34 mm, 37.9 mm and 39 mm thickness on 'Lac Symphonie' and nearby ponds in Metz, France.

A schematic of the experiment is shown in Figure 6.

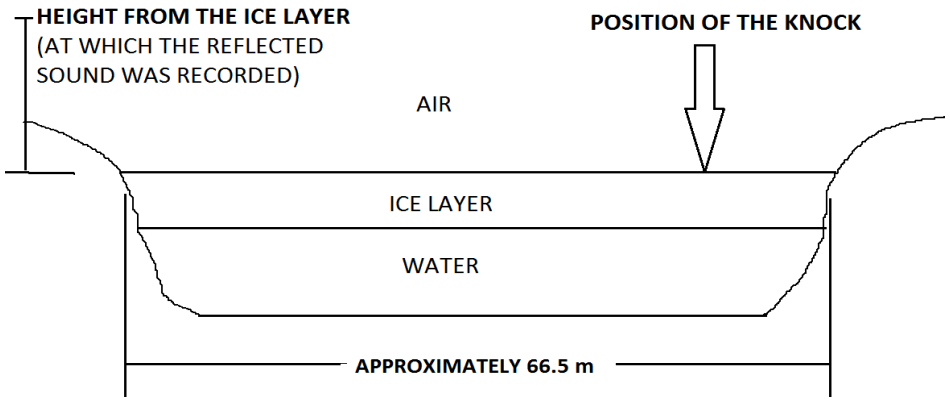

Figure 6: Experimental setup. The height range is 0.5 m - 1.5 m. The width of the 'Lac Symphonie' is calculated to be 66.5 m (± 2 m).

Local conditions play an important role in the growth of the ice thickness. Presence of snow causes damping of acoustic emissions from the ice layer which might cause errors in estimation of the thickness. Hence the experiments were performed when there was no snow on the frozen ice, in order to avoid a muffling (damping) effect on the reflected sound.

2.4 Analysis of the recorded signal

A spectrogram is plotted to analyze the signals for all the thicknesses. As an example, a spectrogram for a 39 mm thick ice layer is shown in Figure 7, with a zoom-in in Figure 8.

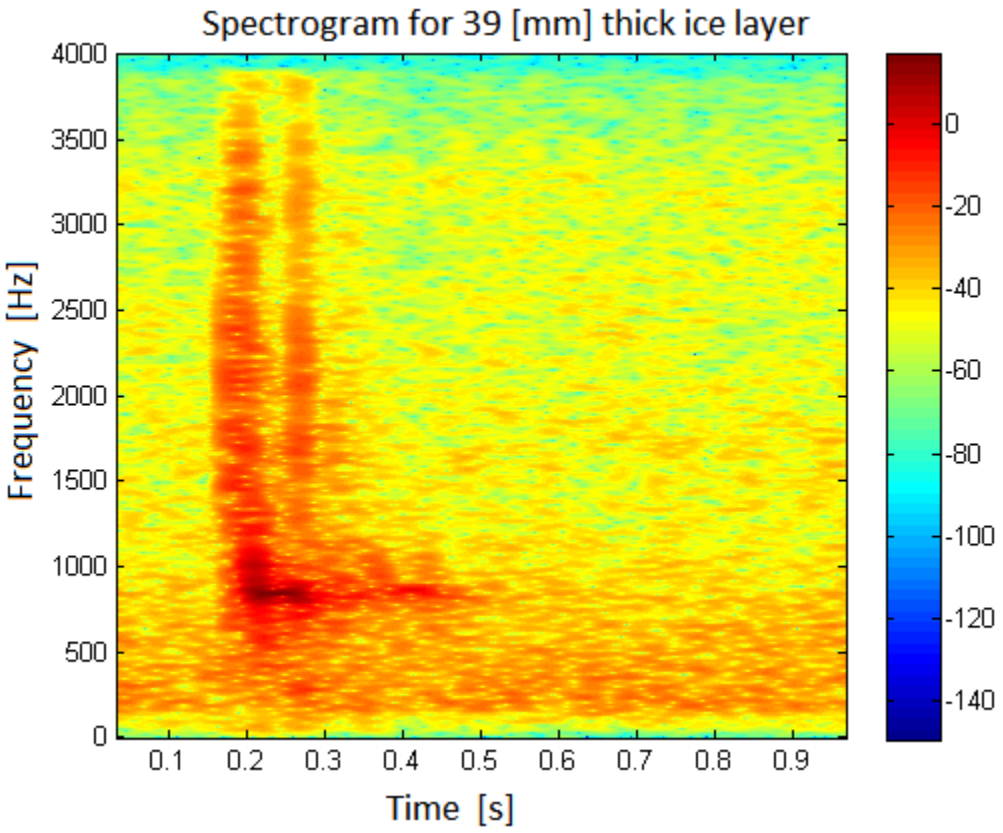

Figure 7: Spectrogram of a pulse recorded at a height of 1.00 m from the ice plate for 39 mm thickness of ice showing the frequencies with high amplitudes in the audio spectrum of the recorded signal for one pulse (i.e. a knock).

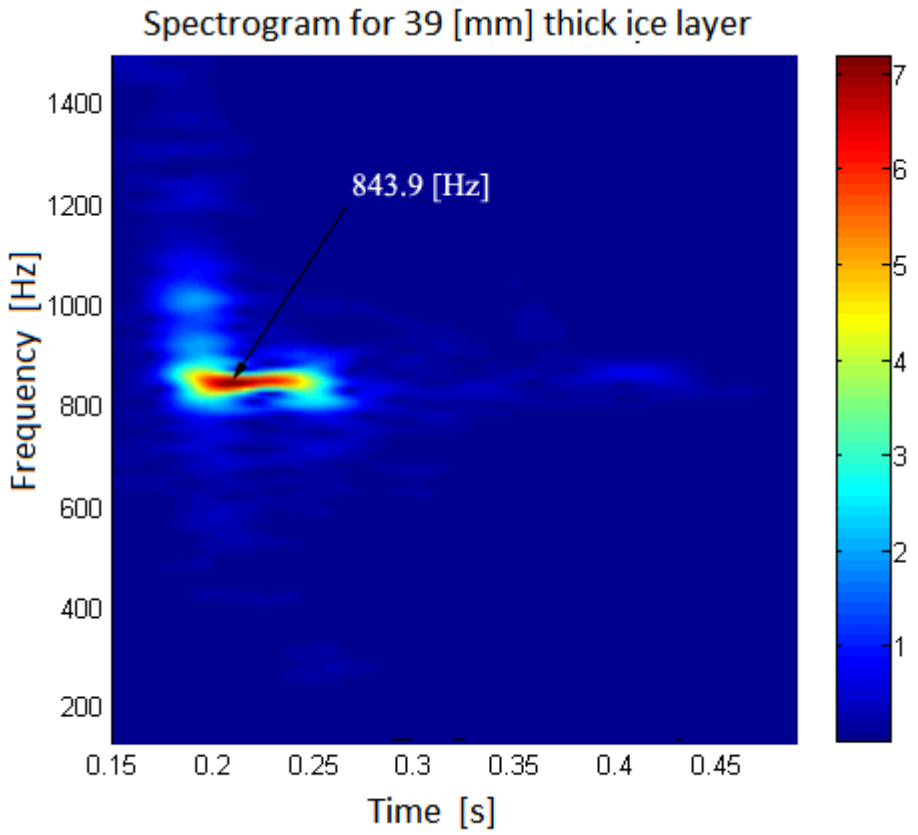

Figure 8: A zoomed representation of Figure 7 which shows the low frequencies showing high amplitudes for a long period of time.

As mentioned earlier, when one knocks or throws a stone on ice, one can hear a fluting sound. This fluting sound is different for different thicknesses of ice. In Figure 7 and Figure 8 the color brightness represents the amplitude. Bright regions represent higher amplitude. There are some high frequencies appearing with high amplitudes but since they appear for a very short span of time i.e. less than a millisecond, they are merely perceived as a 'tic' or are not heard at all by the human ear. On the other hand the lower frequencies revealed in the same Figure7 show high amplitudes and they appear for a longer period of time. Hence these are the frequencies that are heard in the recorded audio by the human ear. In the recorded audio signals one cannot hear just one frequency;

instead one can hear a range of frequencies. In Figure 8 it can be seen that a range of frequencies is showing high amplitudes. The average of this narrow range (820.4 Hz - 867.4 Hz) with high amplitude, appearing for the longest period of time is 843.9 [Hz]. This is considered to be the key frequency that is heard.

The change in height of the recording microphone from the ice layer, and, the horizontal distance between the knock and the recording microphone causes a change in amplitude of the signal but does not affect the range of frequencies being excited. The change in amplitude is well below 10% for a height range of (0.50 m to 1.50 m). The ratio of the amplitudes for different frequencies excited remains the same. If the horizontal distance or the height is too large (i.e. the height is much greater that the average height of a human being and/or the horizontal distance is much larger than the dimensions of the lake) then the amplitude of the fluting noise will be too low to be heard, hence will not useful.

2.5 Appearance of an echo

Apart from a first fluting pulse, one can observe multiple fluting pulses as a result of a knock on ice. In Figure 9 we see a spectrogram of a pulse recorded at a height of 1.00 m from the 28.5 mm thick ice plate (for ‘Lac Symphonie’), showing the frequencies with high amplitudes in the audio spectrum of the recorded signal for one knock.

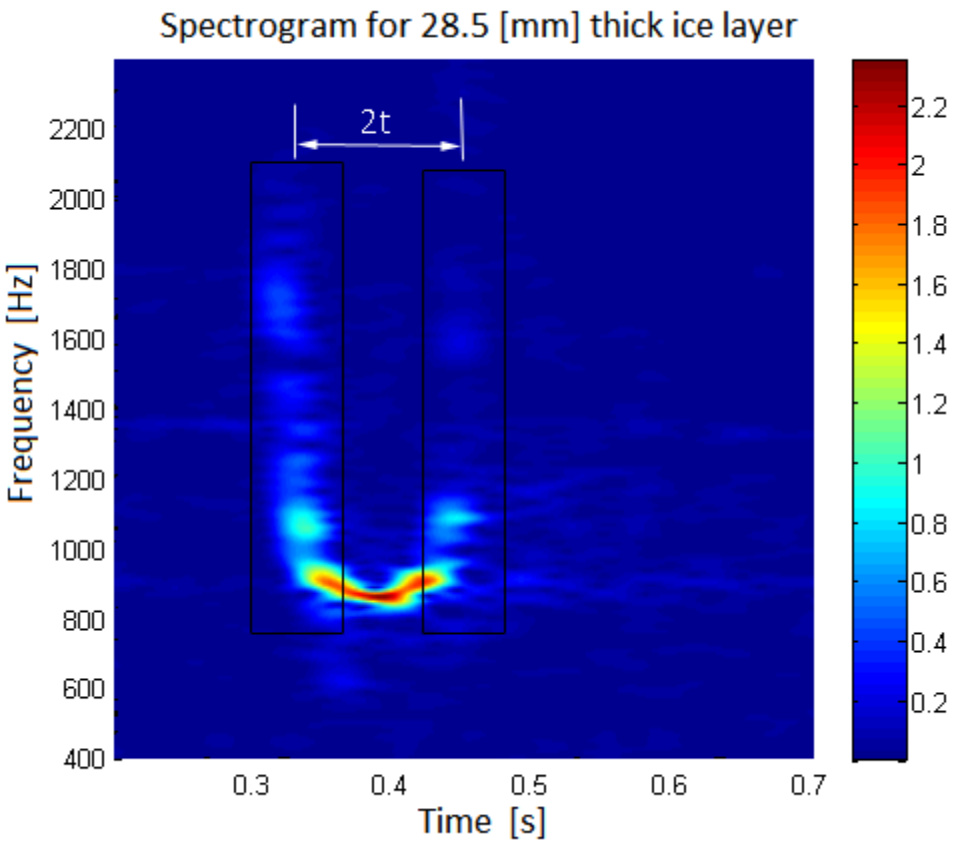

Figure 9: Spectrogram of a pulse recorded at a height of 1m from the ice plate thickness of 28.5 mm, (for 'lac Symphonie') showing the frequencies with high amplitudes in the audio spectrum of the recorded signal for one pulse (i.e. a knock).

Clearly high amplitudes are visible in Figure 9 for a wide range of frequencies appearing at two different times, namely 0.33 s and 0.42 s. The first set at 0.33 s represent the knock and the second set of frequencies with high amplitudes appear due to an echo from the other end of the lake. The distance between the two ends of the lake is calculated using

$$s = c_{water} * (t_2 - t_1)/2$$

Where c_{water} = speed of sound in water 1480 m/s,

t_1 =time at which the 1st set of frequencies heard

t_2 =time at which the 2nd set of frequencies heard

$2t=t_2-t_1$

For this pulse s = 66.5 m. This distance estimation for the echo generation is confirmed using an aerial image of the lake on 'Google maps'.

2.6 Comparison of simulated and experimental results

As mentioned earlier in the work, when one side of the plate is loaded with water, a Scholte- Stoneley wave along with Lamb modes is visible. The experimental results are compared to the results obtained using the analytical model described earlier for the ice thickness of 39 mm.

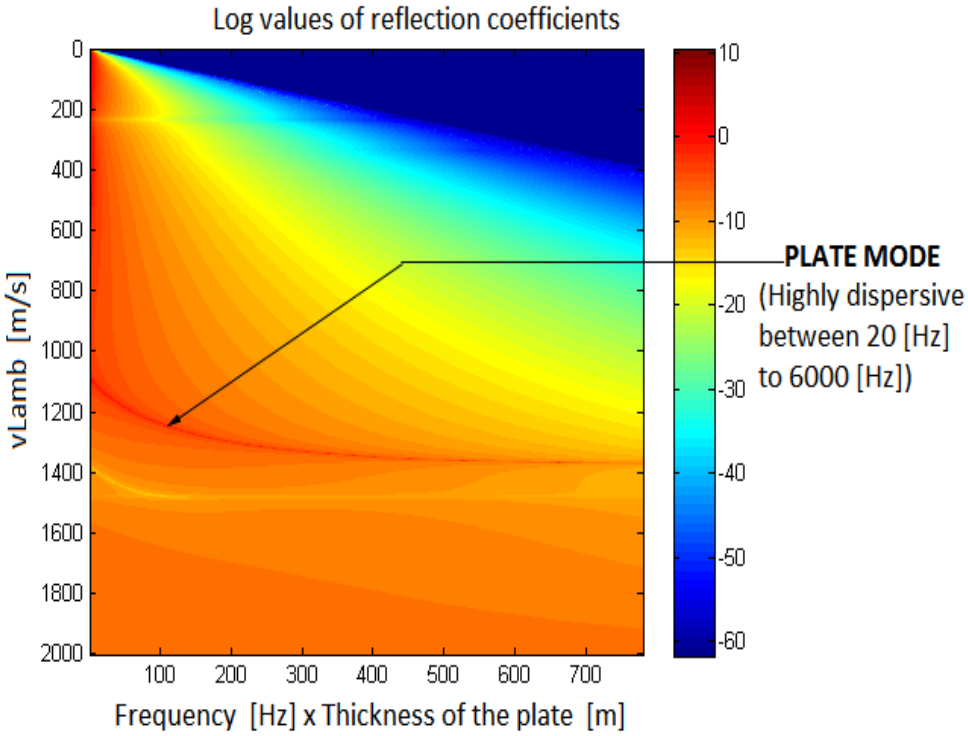

Figure 10: Representation of the reflection coefficients for an ice layer (39 mm in thickness) with air on top and water below for a frequency range 20 Hz - 20 kHz and phase velocity range (0 - 2000 m/s).It is a zoomed representation of Figure 5.

Earlier in this work in Figure 5, one can see a plate mode for low phase velocity, lower than the Rayleigh wave velocity, which closely corresponds to the Scholte- Stoneley wave. In Figure 10, one can see a zoomed image of this mode. It is dispersive for very

low frequencies mainly ranging from 20 Hz – 6000 Hz. From the above simulation results one can see that the exotic features corresponding to the dispersion curves depend on the product (f x d) (i.e. frequency [Hz] x thickness of the plate [m]) as expected in the case of classical Lamb waves.

From the audio signals, recorded for the 39 mm thick ice layer, the average frequency with high amplitude, which is heard for a longer period of time, is extracted. The product of this frequency 'f' and the thickness 'd' of the ice plate generating it is calculated. This $(f \times d)_e$ value ((f x d) value obtained from the experimental results) is compared to the dispersion curves, obtained using the plane wave model described earlier, for the same thickness of the ice layer. This process is repeated for other thicknesses of ice recorded in the experiment. For the respective $(f \times d)_e$ values, the reflection coefficients show a very high amplitude at a particular point on the plate mode described in section 2.1. This particular point corresponds to a phase velocity of 1156 m/s. For thicknesses lower than 0.30 m, this plate mode is the only distinct mode visible in the audible range. The phase velocity is different for different thicknesses of ice. This is true for thick layers but for very thin plates (i.e. plate thickness less than 0.30 m), the phase velocity with the maximum amplitude along the plate mode is found to be 1156 m/s ± 10 m/s. The error in the phase velocity showing maximum amplitude for different thicknesses in the range of 0.03 m -0.30 m is found to be 0.87%. Thus the phase velocity 1156 m/s is used to obtain $(f \times d)_s$ values from the simulated results for different thicknesses. We know that phase velocity of a mode is proportional to the product of the thickness of the plate and frequency. Hence it is possible to have the same phase velocity

for different thicknesses. The $(f \times d)_s$ values for the phase velocity of 1156 m/s, are tabulated along with the $(f \times d)_e$ values, in the following Table 2.

Table 2: Comparison of experimental results and simulated results of (f x d) in [Hz. m] of the plate mode described above.

THICKNESS [m]	**Simulated results $(f \times d)_s$ [Hz.m]**	**Experimental results $(f \times d)_e$ [Hz.m]**	**Percentage error** $\left\lvert \frac{(f \times d)_s - (f \times d)_e}{(f \times d)_s} \right\rvert \times 100\%$
0.029	31.98	27.39	14.35
0.034	32.28	31.75	1.64
0.038	32.49	32.57	0.25
0.039	32.35	32.91	1.73
0.042	32.32	32.55	0.71

The analytical and experimental results for different thicknesses of ice are compared and the error in the (f x d) values is found to be less than 10 % except for an ice thickness of 0.029 m. Since 0.029 m thickness is way below the safe limit (0.10 m), the results for this thickness can be ignored. We are interested in estimating the thickness of ice within the thickness range of 0.03 m – 0.30 m. The percentage errors in the (f x d) values for each thickness are tabulated in Table 2. For an ice plate thickness of 0.039 m, the percentage error in the (f x d) value is -1.73 %. This error could be reduced by adjusting the selection and averaging of the narrow range of frequencies that are heard. We have considered the ice layer in our model to be isotropic and uniformly thick for the simplicity of our problem, but in reality, since ice can be very complex in nature and maybe non uniform

in some areas, it is possible that these complexities and non uniformities contribute to the errors in calculation of the (f x d) values.

2.7 Musical note for every thickness of thin layers of ice

The analytical model described in this earlier, is used to generate $(f \times d)_s$ values for the phase velocity of 1156 m/s. This is done for different thicknesses and the corresponding frequency values are extracted for each thickness.

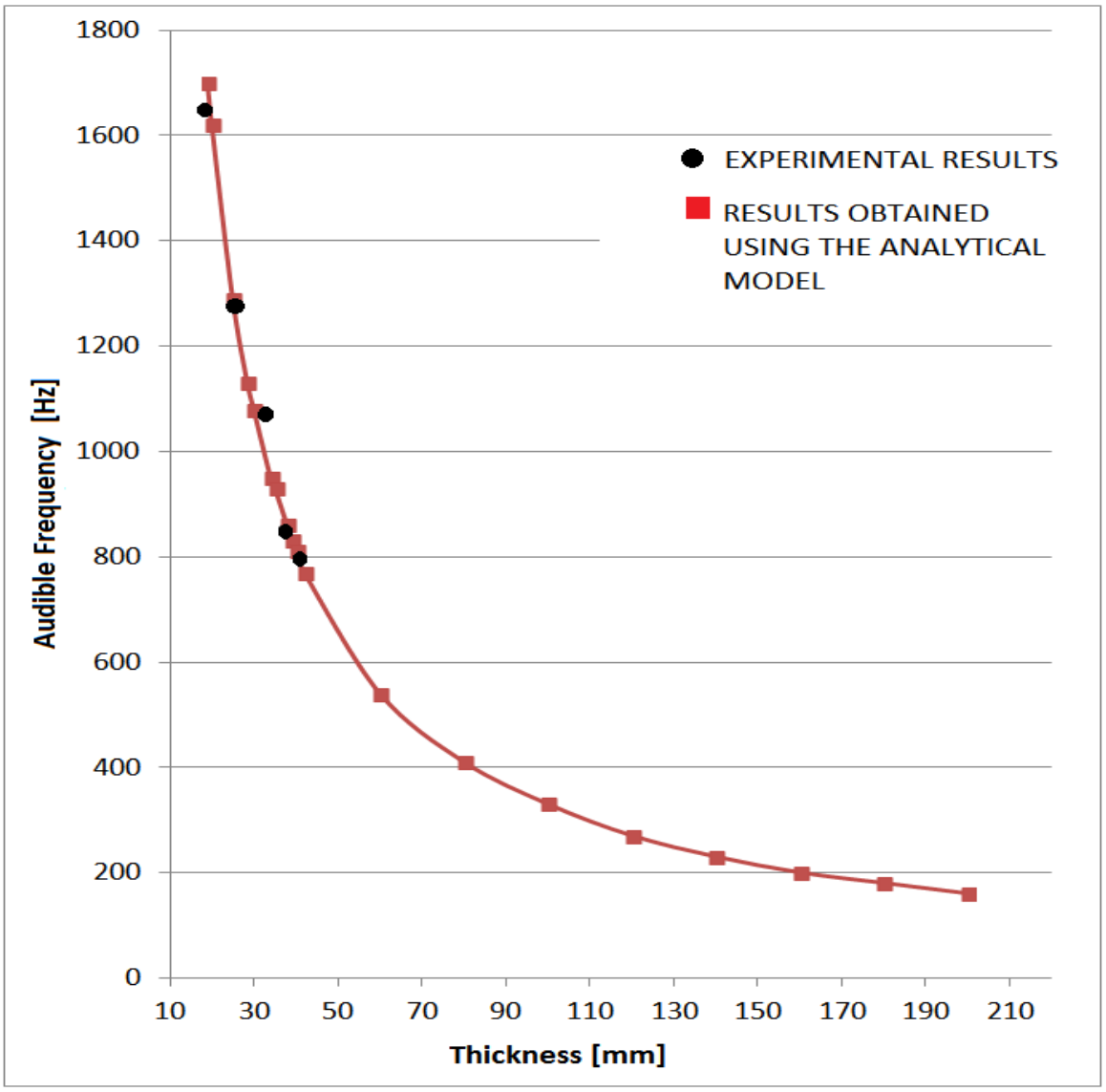

Figure 11: The curve representing the relation between the frequency and the thicknesses of ice.

Figure 11 shows a curve obtained to determine the key frequency for every thickness. It is clear from the curve that the audible frequency tends to decrease with an increase in thickness. For ease of interpretation and use, these frequencies are assigned a musical note using piano key frequencies as shown in Figure 12.

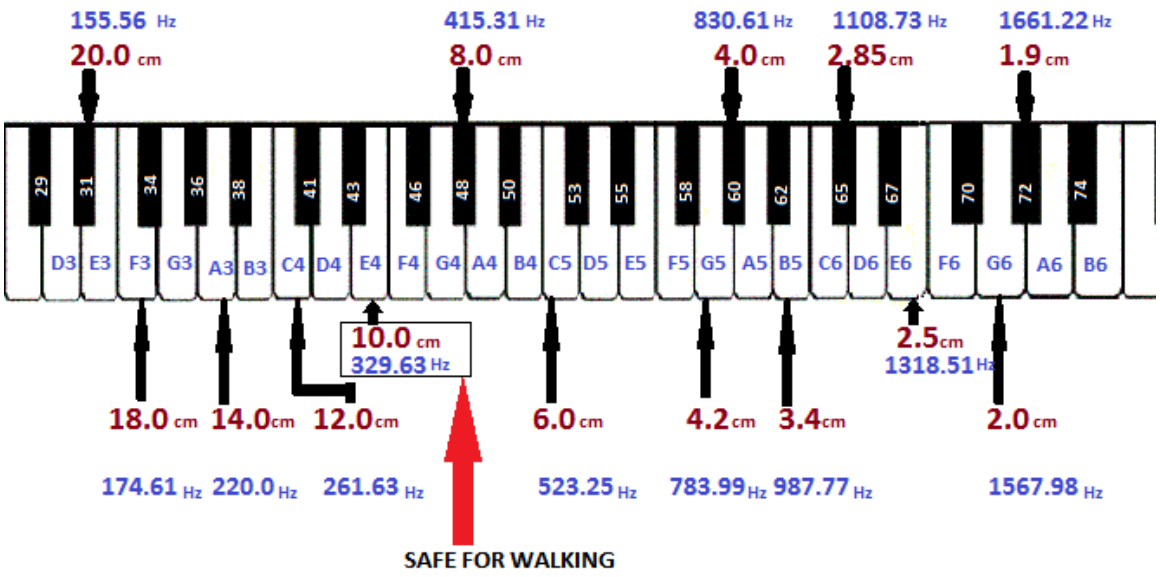

Figure 12: A chart to assign a musical note (key frequencies of a piano) to the thicknesses.

As mentioned earlier in Table 1, 10 cm is suggested to be the safe limit for walking. If one throws a stone on an ice layer of unknown thickness, and can hear a fluting sound whose dominant frequency is less than 329.63 Hz (i.e. a musical note lower than E4), using the chart from Figure12 it can be assured that it is safe to walk on it.

CHAPTER 3

INVESTIGATION OF SOUND DIFFRACTION BY PERIODIC STRUCTURES USING ACOUSTIC MICROSCOPY

3.1 Motivation

Acoustic microscopy can be used to examine the internal structure of an opaque material, without destroying it. Inhomogeneity in the material produces a contrast in the acoustic image, which results from different material densities and acoustic impedances. Information about the material surface and inner layers like microscopic cracks, particles, cavities, voids, and delaminations, and also layer transitions, interfaces or grain structures can be detected using this technique. Acoustic microscopy is a well established technique as far as smooth surfaces are concerned[36-52]. Traditionally V (z) curves are obtained from which, through surface wave generation, important features concerning elasticity and related properties can be extracted. More recently high resolution imaging based on acoustic microscopy has appeared.

A periodic structure can be formed by repeating a unit cell finite or infinite number of times with joined boundaries, in one- dimension, two- dimension or three-dimension. When acoustic waves are incident on such structures, various phenomena; namely, scattering effects, diffraction effects, filtering effects, generation of Scholte-Stoneley waves, etc. are observed. In this work, an attempt is made to characterize different samples with imperfect periodic structures and the possibility of diffraction of sound for high frequencies by samples with nano-structures is explored. These samples are generally used in micro- electronics. They are also used to build LASERs. The

surface profiles of the samples have periodic structures but lack smoothness. The periodicity causes sound diffraction and the roughness influences the acoustic microscopic investigation. Small acoustic contrast between the substrate and the periodic corrugation materials give us information about the additional stresses which develop and affect the bonding between the two materials. In this work, a description is presented of the experiments and a comparison is made between results on smooth surfaces and results on periodic structures of the same material.

3.2 Description of the technique

The Scanning Acoustic Microscope employs the pulse reflection technique. The spatial acoustic objective-centerpiece of the microscope, produces, transmits and receives short sound pulses at high sampling rates. In Figure 13 (a) and Figure 13 (b), we see an acoustic lens in which the high frequency vibrations propagate as a plane parallel wave field inside. These waves are refracted to form a spherical wavefront centered at the focal point of the lens. Water is used as a coupling fluid. Figure 13 (b) shows the focusing effect of the lens. The zenithal angle θ is the angle to the lens axis, taken to be normal to the specimen surface.

Surface waves are generated in the sample. These surface waves (leaky Rayleigh waves) interact with the bulk waves and contribute to the reflected signal. The acoustic lens receives the sound pulses reflected from the sample and the transducer converts it into electromagnetic pulses which are displayed as pixels with defined gray scale values. To produce an image the acoustic scanner vibrates along the x direction and sweeps along the y direction line by line. The image is formed by the transducer scanning mechanically over the sample. The scanner is lowered in the z direction to focus on the inner layers of

the sample. Using acoustic images obtained for different z positions a V (z) curve can be plotted for different positions. Appendix B provides a detailed description of the scanning acoustic microscope.

The V (z) curve can be extracted for any point on the sample surface, from the scanned acoustic images. These curves are analyzed to measure several local visco-elastic parameters of the sample; namely modulii of elasticity, viscosity coefficients, shear and longitudinal velocities, etc.

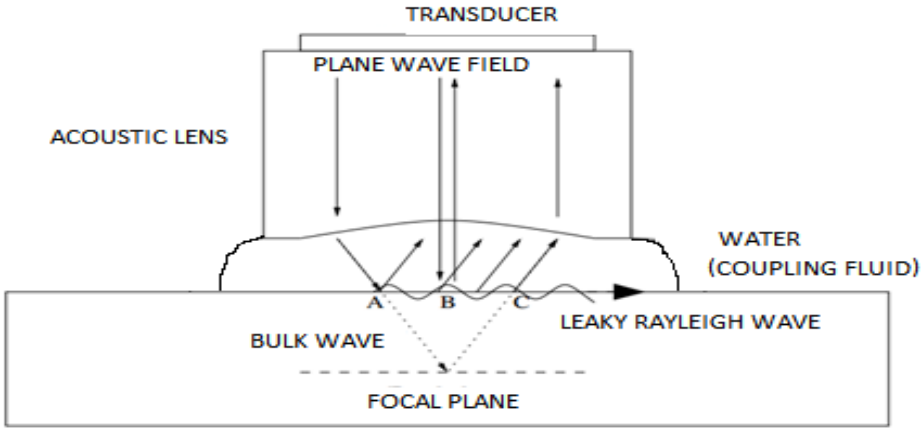

Figure 13 (a): Schematic representation of the Scanning Acoustic Microscope.

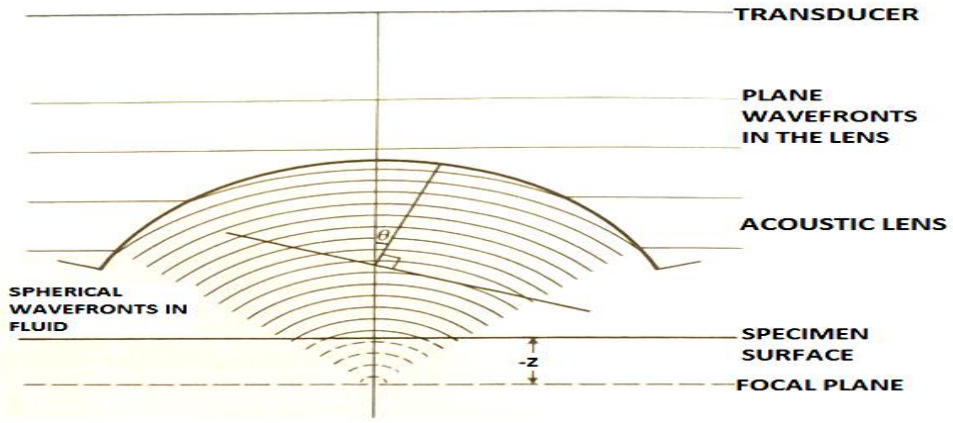

Figure 13 (b): Diagrammatic representation of the wave model of an acoustic lens showing the focusing effect.

3.3 Experiments and discussion

3.3.1 Periodic structures on Brass

The sample investigated here is a brass sample with grooves. The sides of the top surface of the sample, appears to be fairly smooth to the naked eye, as seen in Figure 14 (a), which shows an image of the sample taken by the camera. The central part has grooves cut out in the sample with a periodicity Λ equal to 178 μm. Figure 14 (c) shows a diagrammatic representation of the corrugation. The top surface of the groove is referred to as the valley and the top surface of the side walls is referred to as the hill. Figure 14 (b) shows an image of the sample obtained using an optical microscope. Using this image, the width of the hill is measured. Some surface defects like scratches and dents are visible on the plane surface. Figure 14 (d) shows an acoustic image of the sample surface scanned using the SAM. In this image, the acoustic contrast due to imhomogeneties on the surface, make the surface defects clearly visible not only for the plane surface, but also the surface of individual hills. Individual hills and valleys, appear to be of uniform width and smooth edges in the Figure 14 (a) and Figure 14 (b), whereas, the acoustic image in Figure 14 (d) shows that edges of the hill are extremely rough and the width of the hills and valleys vary. The width for one hill, as shown in Figure 14 (d), is measured to be 65.7 μm ±2.5 μm. All measured values are rounded off to one significant figure after the decimal.

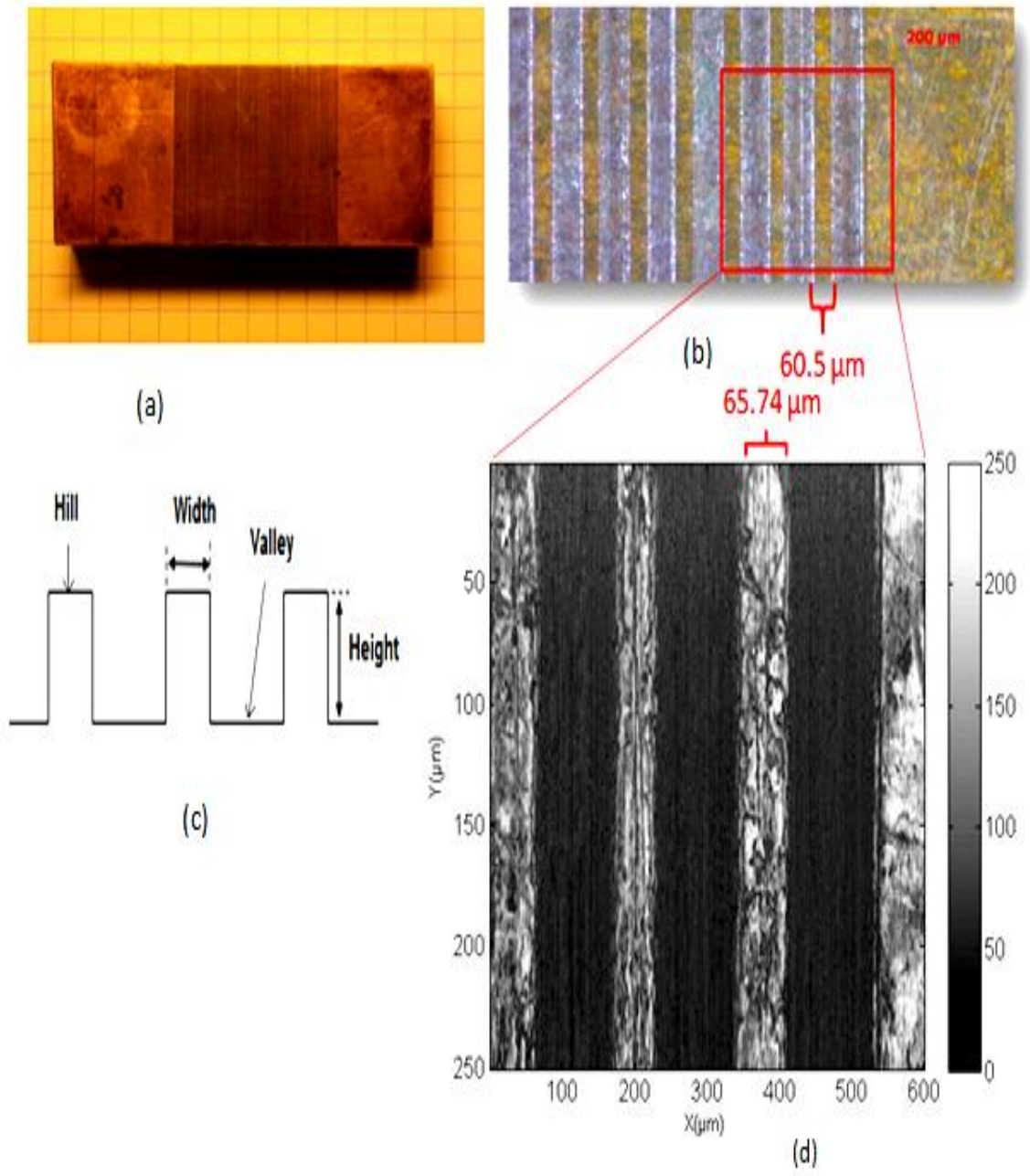

Figure 14: (a) Image of the brass sample taken by a camera, (b) Image obtained using an optical microscope, (c) Diagrammatic representation of a section of the sample and (d) Image obtained using SAM. Transducer frequency used is 400 MHz.

3.3.1.1 *Hill height estimation*

Images produced using an optical microscope or a scanning electron microscope can give us a lot of information about the surface. The width of the hills and grooves of

this sample can be easily measured by these tools, but it is difficult to make a good estimate of the height of these hills using them. In this work, the scanning acoustic microscope is used for material characterization of this sample which includes not only the estimation of the periodicity and estimation of the width of the hill, but also the height of the hill. The sample is scanned using the SAM for different z positions. V (z) curves are plotted for a position on the top plane surface with no grooves and a position on the valley (or the bottom surface) respectively.

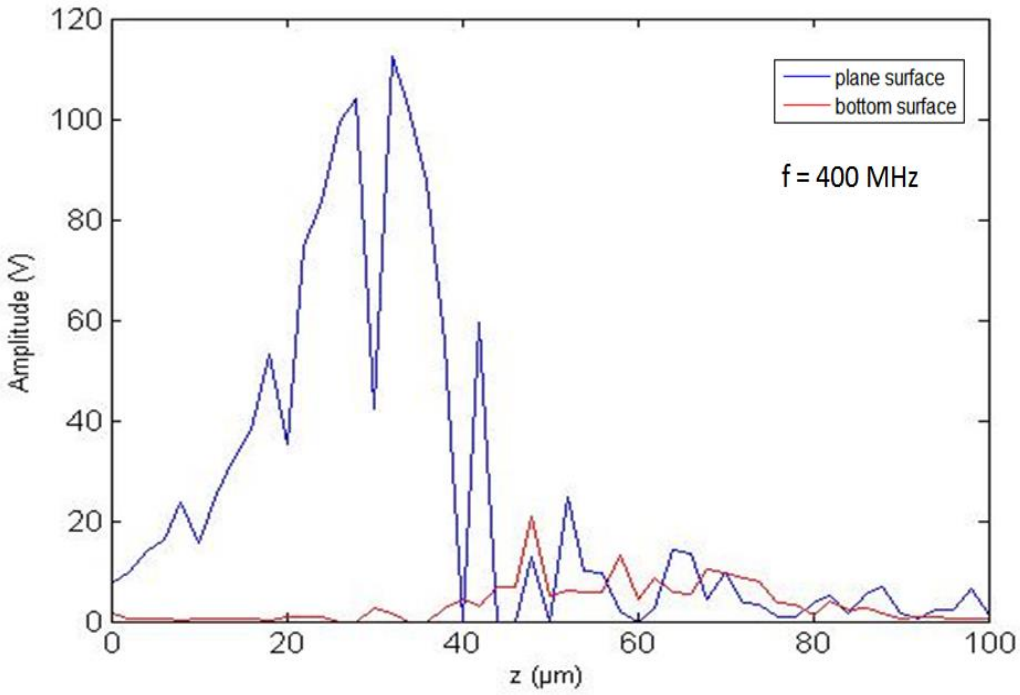

Figure 15: V (z) curve for the brass sample. Transducer frequency used is 400 MHz.

In Figure 15, the curve in blue represents the V (z) plot for the top plane surface, and the red curve represents the V (z) plot for the position on the valley. A 400 MHz focused transducer is used for the experiment. When the transducer is focused on the top surface of the hill on the sample, the reflection amplitude is maximum. Similarly, when the transducer is focused on the top surface of the valley on the sample, the amplitude of

the received signal is maximum. The initial z position of the scan in Figure 15 is the same defocused position for both cases. The two curves are compared and the distance between the positions for which we have the maximum amplitude, for the respective curves, gives us a measure of the height of the hill. This process is repeated for two cases. In case 1, V (z) curves for thirty different positions (x, y) on the valley is compared individually with the V (z) curve for the same position (x, y) on the plane surface. In case 2, V (z) curves for thirty different positions (x, y) on the plane surface, is compared individually with the same position (x, y) on the valley.

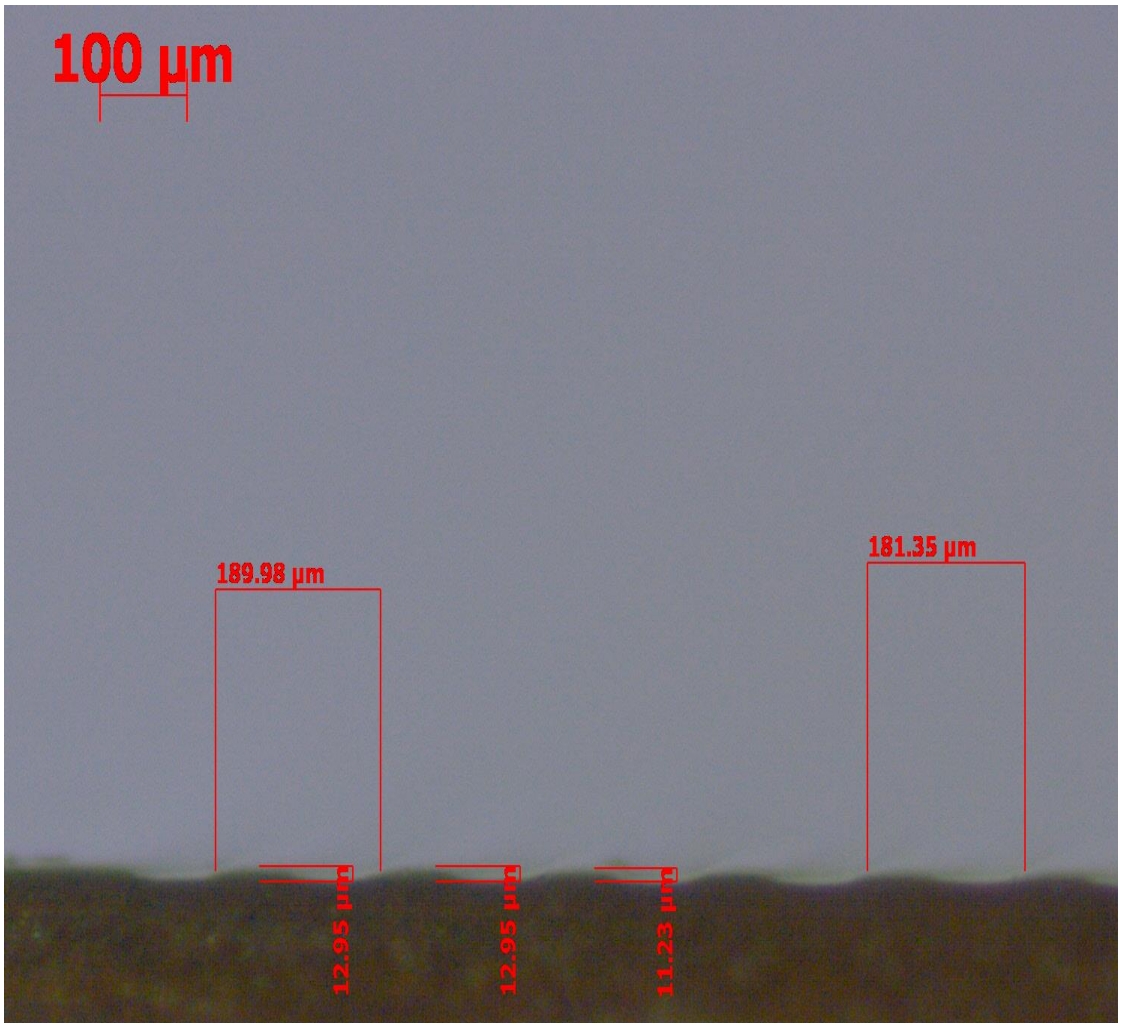

Figure 16: Side view of the sample obtained using an optical microscope.

A rough estimation of the hill height is made from the optical image in Figure 16 and compared with the height value for the same hill, calculated using the V (z) curve technique.

Table 3: Comparison of the calculated hill height for case 1 (different positions on the valley) and case 2 (different positions on the plane surface).

	Hill Height (µm)	
	Case 1	**Case 2**
1.	12.9	10.2
2.	12.8	14.2
3.	12.8	12.6
4.	10.8	11.3
5.	13.2	12.4
6.	12.8	11.3
7.	12.8	12.6
8.	11.3	10.9
9.	12.8	12.6
10.	12.8	11.3
11.	14.8	12.6
12.	10.8	12.6
13.	12.8	12.6
14.	12.8	12.8
15.	12.8	12.6

Table 3 continued

16.	11.4	13.2
17.	13.2	12.6
18.	12.8	12.6
19.	11.4	12.6
20.	12.8	12.6
21.	10.9	11.9
22.	12.8	12.8
23.	12.2	12.4
24.	12.8	12.6
25.	11.2	11.8
26.	12.8	12.6
27.	12.8	12.8
28.	12.8	12.6
29.	11.3	12.3
30.	12.8	12.6
Mean	12.4	12.4
Median	12.8	12.6
Mode	12.8	12.6

Table 4: A comparison between the hill heights and hill widths respectively, obtained from an acoustic image and optical image.

Frequency	Hill Width (μm)	Hill Height (μm)	
		Different Positions on the valley	Different positions on the plane surface
400 MHz	65.7 ± 5.0	12.8 ± 2.0	12.6 ± 2.4
Optical image	60.5	13.0	

From Table 3, the mean value, the median value and the modal value of the list of data for the hill height is calculated for case 1 and case 2. All values are rounded off to one significant figure after the decimal. The modal values (12.8 μm for case 1 and 12.6 μm for case 2) are compared to the estimated values obtained from the optical image in Table 4. The hill height for case 1 ranges from 10.8 μm to 14.8 μm. For case 2, it ranges from 10.2 μm to 14.2 μm. The hill width obtained from the acoustic image using a 400 MHz transducer, lies within the range of 65.7 μm ± 5.0 μm along the length of the hill in the y direction, where the modal value is 65.7 μm. The modal value of the hill width for the same hill was calculated using data for thirty different positions along the length of the hill.

3.3.1.2 *Reliability check*

The FFT of the V (z) curves plotted in Figure 15 are plotted in Figure 17. In order to check if the V (z) curves are correct, the longitudinal velocity, the shear velocity and the shear modulus are calculated using these curves.

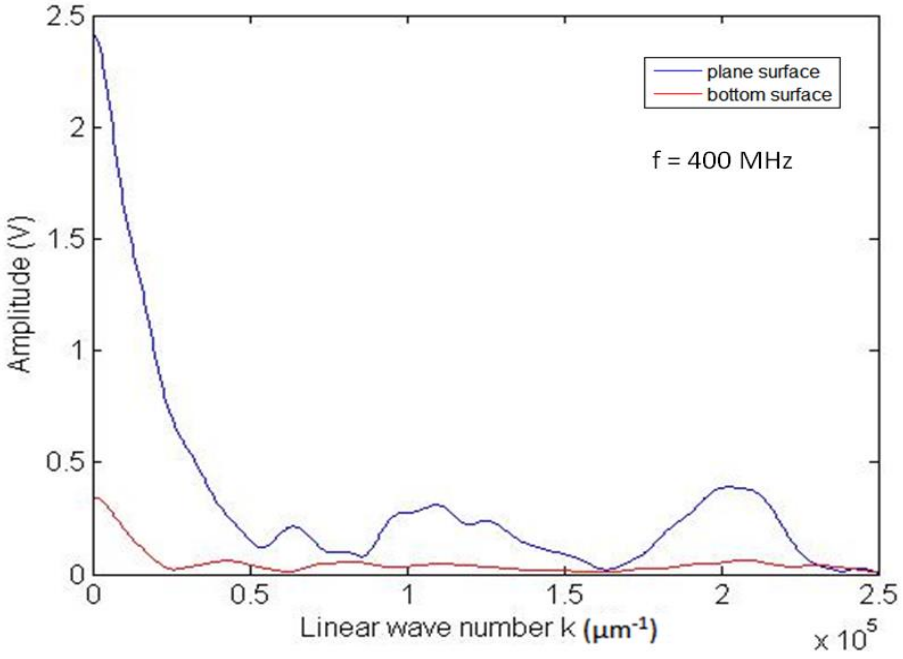

Figure 17: FFT of the V (z) curves. Transducer frequency used is 400 MHz.

From the blue curve representing a position on the plane surface, the single frequency corresponding to the interpolated maximum amplitude is chosen as the spatial frequency and is used to calculate the above mentioned quantities using the following equations:

$$\mathbf{v_l^2} = \frac{\boldsymbol{\lambda + 2\mu}}{\boldsymbol{\rho}} \quad (46), \quad \mathbf{v_s}^{\mathbf{2}} = \frac{\boldsymbol{\mu}}{\boldsymbol{\rho}} \quad (47)$$

$$\mathbf{v_s} = \frac{2f_c}{\boldsymbol{\nu}_{osc}} \quad (48)$$

where v_l , v_s , $\boldsymbol{\nu}_{osc}$ and f_c are longitudinal velocity, shear wave velocity, spatial frequency and central frequency respectively. $\boldsymbol{\rho}$ is the density of the sample. In this work, the density of brass used is 8651 kg/m^3.

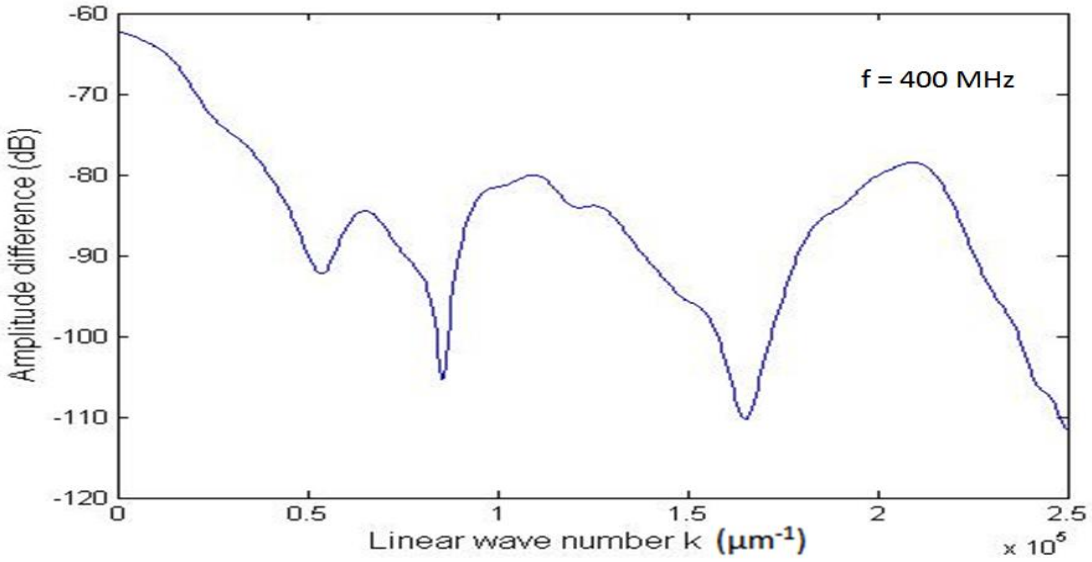

Figure 18: A plot of the difference between the FFT curves in figure 17.

Figure 18 shows the difference between the two FFT curves in Figure 17, plotted in dB scale. This is done to remove the effects due to the material properties and to focus on the change in amplitude due to the corrugation. The spatial frequency with the highest amplitude in Figure 18 corresponds to the spatial frequency with maximum amplitude in Figure 17, which is used to calculate the shear velocity in the brass sample.

Table 5: Estimation of the longitudinal velocity, shear velocity and the shear modulus for different transducers.

Frequency (MHz)	**Longitudinal Velocity (m/s)**	**Shear Velocity (m/s)**	**Shear Modulus (GPa)**
400	4136.34 ± 172.45	2282.62 ± 167.45	45.07 ± 13.55
5	4259	2341	47.40
Percentage Difference	2.9%	11.1%	5.8%

A low frequency transducer with a frequency of 5 MHz is used to calculate the longitudinal velocity, the shear velocity and the shear modulus using the time of fight method. These values are compared with the values obtained from the V (z) curve. The percentage difference is well within 10%.This confirms that our technique of estimation is sound and consistent.

3.3.1.3 *Error estimation*

The measured value R is considered to be a function of independent variables, $x_1, x_2 \ldots, x_n$, defined by

$$R = f\{x_1, x_2 \ldots, x_n\} \quad (49)$$

Where n is the number of independent variables. Each variable contains some measure of uncertainty and hence affects the result. The best estimate of the true mean value R' is given by

$$R' = \bar{R} \pm u_R \quad (50)$$

where $\bar{R}$ is the sample mean, and u_R is the uncertainty in R given by

$$u_R = \pm \sqrt{\sum_{i=1}^{n} \left(\frac{dR}{dx_i}\right)^2} \quad (51)$$

This technique is used to calculate the values in Table 3 and Table 5. The values for the 400 MHz transducer represent an estimate of the true mean value, obtained from thirty sets of data, i.e. thirty different positions on the sample surface. The percentage difference is well within 10%. This confirms that our technique of estimation is sound and consistent. As mentioned in Appendix B, the scanning acoustic microscope has

limitations and shortcomings which the manufacturers need to fix. These shortcomings also add to the error in measurement and calculation.

3.3.1.4 *Diffraction of sound*

For high frequencies, the attenuation is high, hence diffraction of sound is difficult to observe. In Figure 19, the two V (z) curves representing attenuated reflected signals from the plane surface and the corrugated surface, respectively, are compared and a significant amplitude difference is observed. In other words, the reflected signal from the corrugated area, i.e. the red curve, shows a significant amplitude drop, when compared to the blue curve. This drop in amplitude is caused due to the scattering of sound.

The periodicity of the corrugation needs to be of the same order as the wavelength of the incident wave, in order to have diffraction. The wavelength of the incident wave for the brass sample is 3.75 μm and the periodicity of the corrugation is 178 μm. The periodicity in this case is too large compared to the wavelength hence diffraction due to this corrugation is not possible. The significant amplitude drop observed, is caused due to scattering of sound by the roughness of the surface which is imperfectly periodic and was created during the manufacturing process.

3.3.2. Periodic structures on Sapphire

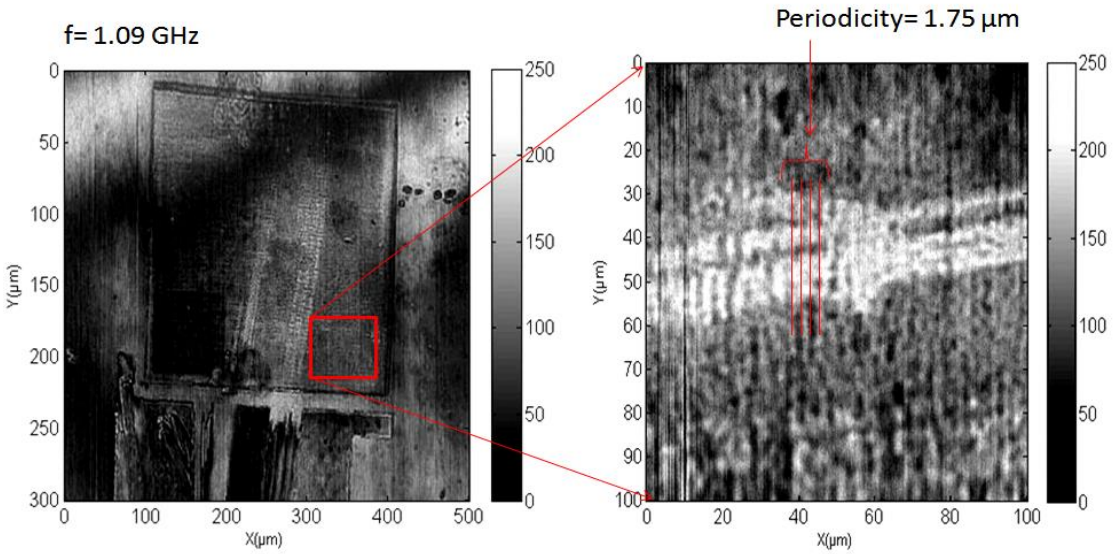

Figure 19: (a) An acoustic image of the corrugated area. (b) A small section of the corrugated region selected from the image 19 (a).

The sample investigated here is a thin layer of sapphire. It is 2.7 mm thick. The material used to create the corrugation on this sample is GaN (Gallium Nitride).

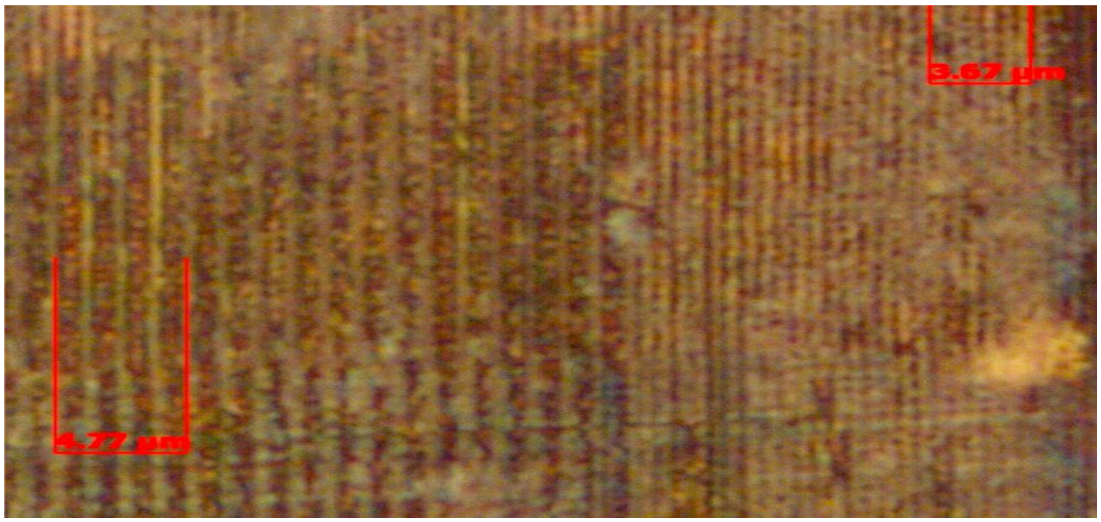

Figure 20: An optical image of the corrugated region on the sample surface obtained using an optical microscope.

The periodicity of the corrugation on the Sapphire sample is significantly lower than that on the brass sample used above. Figure 19 (a) shows an acoustic image of the sample obtained using the SAM. A small section from the corrugated area with fairly uniform periodicity is scanned, as seen in Figure 19 (b). The periodicity is calculated from Figure 19 (b) to be 1.75 μm. The transducer frequency used to obtain the acoustic images in Figure 19 is 1.09 GHz. The periodicity calculated using an optical image in Figure 20 is 1.5 μm. The percentage difference in the two values is 16.6 %.

As mentioned earlier, SEM and optical microscopes give a good estimation of the periodicity and the surface of the sample layer. This sample is very thin (2.7 mm thick) compared to the brass sample discussed in the previous section; hence it is not possible to estimate the height of the corrugation for this, at all. This is where the technique discussed in this work proves useful.

3.3.2.1 *Hill height estimation*

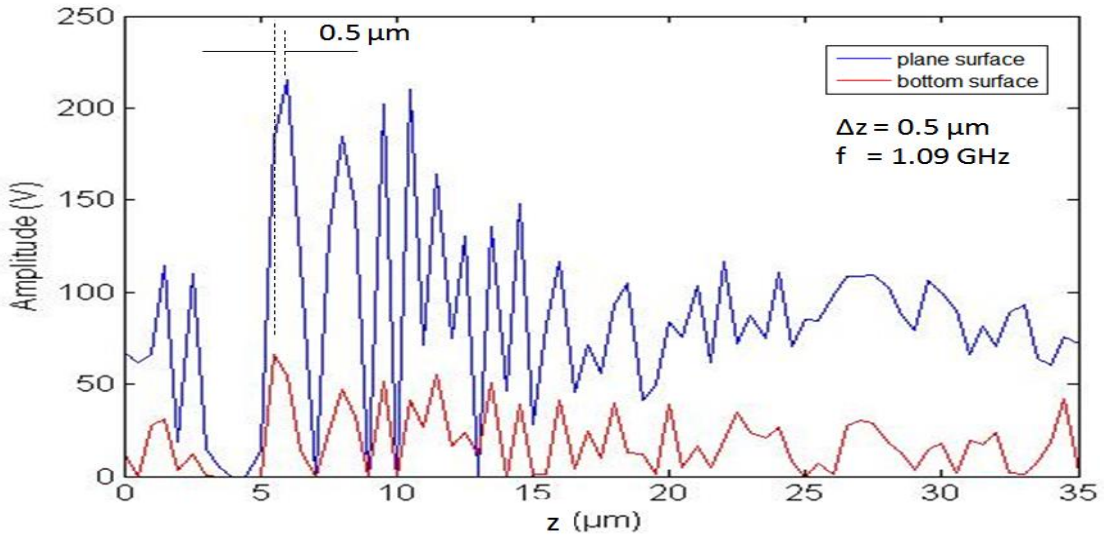

Figure 21: V (z) curves for the periodic structures on Sapphire. The transducer frequency used is 1.09 GHz.

The sample is scanned using the SAM to obtain acoustic images for different depths, i.e. different z positions. Two V (z) curves are plotted in Figure 21. The blue curve represents the V (z) curve for a position (x, y) on the plane surface with no corrugation. The red curve represents the V (z) curve for a position (x, y) on the corrugated region. The starting z position for the acoustic scan is a defocused position where the transducer focuses on a z position above the sample surface. After every scan, the transducer is lowered towards the sample surface, i.e. in the positive z direction.

The resolution in the z direction, or in other words, Δz, used to obtain the V (z) curves is 0.5 μm. Using the same technique as described in section 3.3.1.1 above, the approximate height of the corrugation is estimated to be 0.5 μm as seen in Figure 21. Since the height and the resolution in the z direction are equal, we can conclude that the height is less than 1 μm. It might be possible that the difference in z positions with maximum amplitudes for the two curves is a result of a mechanical error of the system. In order to check if the height estimation was correct, the resolution in the z direction was increased to 0.3 μm.

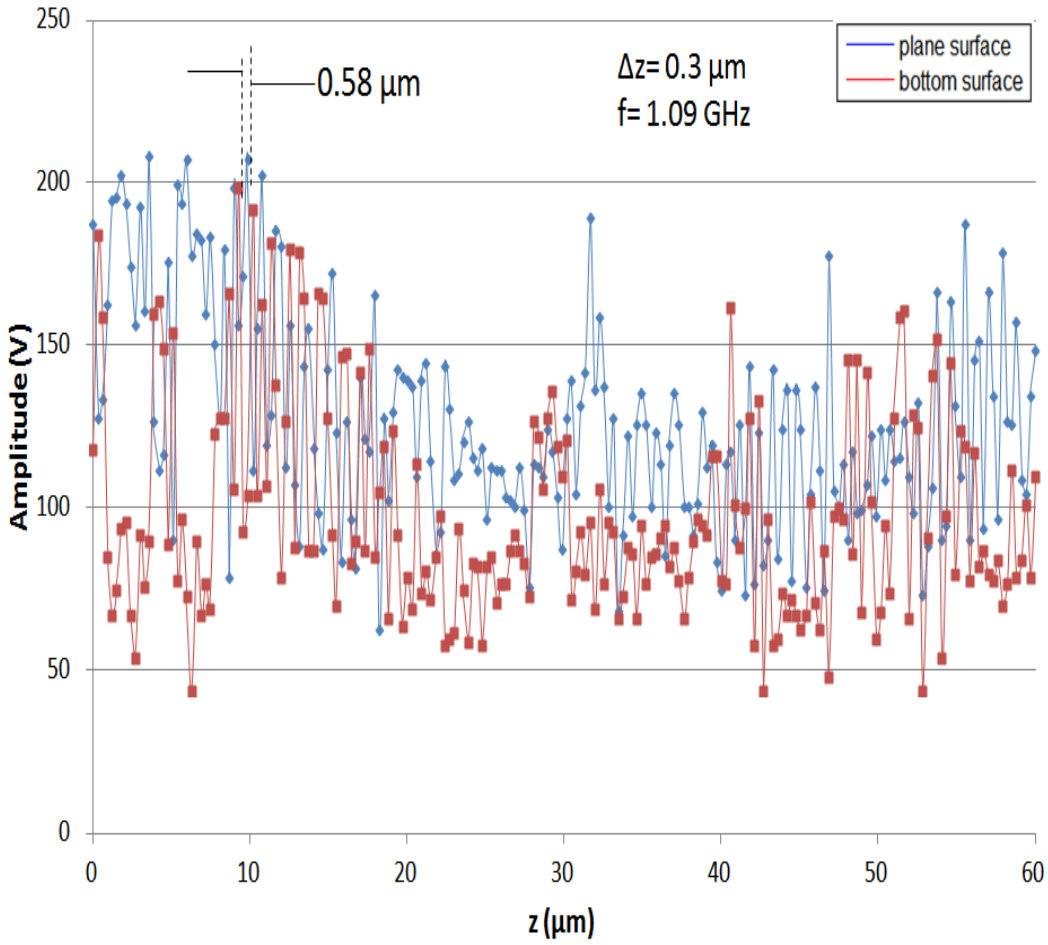

Figure 22: V (z) curves for the periodic structures on Sapphire for a resolution of 0.3 µm in the z direction.

In Figure 22, the two V (z) curves obtained using a higher resolution in the z direction, are compared. The hill height is estimated to be 0.58 µm. This process is repeated for two different cases. In case 1, the hill height is estimated for thirty different positions on the valley and the same position on the plane surface. In case 2, the hill height is estimated for thirty different positions on the plane surface and the same position on the hill of the corrugation.

Table 6: Comparison of the calculated hill height for case 1 (different positions on the hill) and case 2 (different positions on the plane surface).

	Hill Height (µm)	
	Case 1	**Case 2**
1.	0.58	0.43
2.	0.58	0.48
3.	0.93	0.54
4.	0.56	0.65
5.	0.53	0.58
6.	0.55	0.56
7.	0.63	0.55
8.	0.45	0.50
9.	0.58	0.49
10.	0.42	0.69
11.	0.56	0.58
12.	0.56	0.57
13.	0.53	0.58
14.	0.59	0.58
15.	0.58	0.56
16.	0.62	0.58
17.	0.44	0.57
18.	0.53	0.54

Table 6 continued

19.	0.45	0.52
20.	0.55	0.58
21.	0.58	0.43
22.	0.58	0.56
23.	0.59	0.56
24.	0.52	0.62
25.	0.58	0.54
26.	0.54	0.54
27.	0.57	0.58
28.	0.68	0.58
29.	0.42	0.63
30.	0.54	0.52
Mean	0.56	0.56
Median	0.56	0.56
Mode	0.58	0.58

Table 7: A comparison between the hill heights and periodicities respectively, obtained from an acoustic image and optical image.

Frequency	**Periodicity (μm)**	**Hill Height (μm)**	
		Different Positions on the valley	**Different positions on the plane surface**
1.09 GHz	1.8	0.6 ± 0.26	0.6 ± 0.13
Optical image	1.5	-	

From Table 6, the mean value, the median value and the modal value of the list of data for the hill height is calculated for case 1 and case 2. In Table 7, all values are rounded off to one significant figure after the decimal.

Table 8: Specification of the setup and calculated results for the Sapphire sample.

Corrugated area	GaN deposition on Sapphire substrate
Periodicity of the corrugated area	1.75 µm
The SAM resolution in the z direction	0.30 µm
The SAM resolution in the y direction	0.20 µm
Calculated height of the corrugation	0.58 µm
Central frequency of the focused transducer used	1.09 GHz
Wavelength of the incident wave	1.45 µm
Coupling medium	Water

3.3.2.2 *Reliability check*

Table 9: A comparison of the estimated longitudinal velocity, shear velocity and the shear modulus with the known values.

Frequency (GHz)	**Longitudinal velocity (m/s)**	**Shear velocity (m/s)**	**Shear modulus (Gpa)**
1.09 GHz	11800 ± 132.4	6436.23 ± 127.4	160.03± 12.2
Known Values[51]	10000	6240.57	155.1

Using the same technique as mentioned in section 3.3.1.2, the spatial frequency is extracted from the FFT curves. It is used to calculate the longitudinal velocity, the shear wave velocity and the shear modulus, and is compared to the known values to check the correctness of the V (z) curves. The estimated mean values for the respective quantities are calculated using the error estimation technique discussed in section 3.3.1.3. The results are shown in Table 9. All calculated values are rounded off to one significant figure after the decimal. The percentage differences between the known values[51] and estimated values for the respective quantities are well within 10% of the known values. Hence we know that the technique is consistent for high frequencies and for samples with higher periodicity.

3.3.2.3 *Diffraction of sound*

For this sample, the periodicity of the corrugation and the wavelength of the incident wave are very high and of the same order, as seen in Table 10, hence diffraction of sound is possible.

The grating equation states,

$$m\lambda = d\,(\sin\theta_i + \sin\theta_r) \quad (52)$$

where m is the order of diffraction, λ is the wavelength of the incident wave, θ_i is the angle of incidence, θ_r is the angle of diffraction and d is the periodicity.

The grating equation is used to calculate the possible diffraction orders for this particular sample. The transducer frequency used is 1.09 GHz and the semi-aperture angle ranges from 30º to 50º. The possible diffraction orders are +1 and +2.

In Figure 21 for $\Delta z = 0.5$ μm, and in Figure 22 for $\Delta z = 0.3$ μm, the two V (z) curves representing attenuated reflected signals from the plane surface and the corrugated

surface, respectively, are compared. In both figures, a significant drop in amplitude of the reflected signal is observed when the corrugated area is scanned. This drop is due to the scattering effect caused by the corrugation.

CHAPTER 4

CONCLUSION AND FUTURE WORK

In the first chapter, some background information about flexural waves in ice has been presented stating the problem, listing the properties of ice and the conventions currently used to allocate a weight allowance to the thickness of ice. A brief history about acoustic microscopy and diffraction of sound by periodic structures has also been discussed.

The second chapter describes the analytical model used to calculate the reflection and transmission coefficients of sound through ice. Knocking on ice has been simulated by making the generally valid assumption that any sound source can always be described as a combination of plane waves, whence the focus has been on plane wave interactions and dispersion effects as is often done in Lamb wave analysis. In addition, nonlinear effects have been ignored.

Results have been shown for sound being reflected off the ice layer with or without reflection from the bottom of the lake. It has been shown that a good correspondence between the numerical simulations and the experiments is obtained when sound can reflect off the bottom of the lake. Results have been reported for a receiver height of 1.00 m; nevertheless for other heights we found results that show only negligible differences with those at 1.00 m. Furthermore the main sound waves heard for a long duration and perceived as a fluting sound, appear to correspond to waves, referred earlier by Sessarego et al[18] and Destrade[20], as Scholte-Stoneley waves. Sound perceived

as a ‘tic’ is attributed to a very short time period (less than a millisecond) during which a wide spectrum pulse appears in the recording.

An echo, appearing in the experiments, has been correctly explained as reflections from the sides of the lake and this has been confirmed by distance calculations based on aerial maps. For reasons of practical use a correlation found between the main frequencies in the observable ‘fluting’ sound and the thickness of ice has been represented by piano keys. For the specific thickness of 10 cm, which is normally considered as the safety limit to allow crowds to walk on ice, the E4 piano key has been determined as the musical note for the fluting. Frequencies higher than the E4 key correspond to ice thinner than 10 cm. Therefore by knocking on ice or throwing a stone on ice and by listening to the musical note it results in, one can determine the thickness of the plate and assess if it is safe to walk on it or not without the use of any expensive equipment or time-consuming procedures.

In the third chapter, experiments conducted on samples with periodic structures of different periodicity using the scanning acoustic microscope for different spatial resolutions and different transducer frequencies (400 MHz and 1.09 GHz) are presented. The specifications of the scanning acoustic microscope used for these experiments, are presented stating the procedures used for data acquisition in Appendix B. The limitations of the microscope are also discussed. The first step towards our research in acoustic microscopy was to optimize our experimental setup to meet our requirements to obtain reliable results. Once that was achieved, keeping in mind the limitations of the scanning acoustic microscope, experiments were conducted. Longitudinal velocity, shear velocity and shear modulus are calculated using the V (z) curves obtained from the C-scans of the

respective samples to check the reliability of the technique. A technique to estimate the height of the corrugation (difficult to measure using an optical microscope) is described.

A lot of research has been done earlier by several researchers to describe diffraction of sound using low frequency ultrasound but it is difficult to quantify diffraction of sound for high frequencies since the attenuation is very high. In this work an attempt has been made to investigate diffraction of sound and the scattering effect by periodic structures with high periodicity (micron level) for high frequencies. Spatial frequency spectrums obtained from V (z) curves using the technique mentioned in chapter 3 show an indication of diffraction of sound for high frequencies.

Further investigation and analysis of the spatial frequency spectrum are required in order to quantify the diffraction of sound by corrugated structures for high frequencies. Further improvements in the scanning acoustic microscope are required to improve the resolution of the system and the accuracy of the results.

APPENDIX A

STRESS AND DISPLACEMENT EQUATIONS FOR ELASTIC WAVES IN ICE

Using the plane wave model, the displacements can be expressed as:

$$\bar{u}_{x,1} = k_x(P(\cos(K_{z,1}(z - z_s)) + \sin(K_{z,1}(z - z_s))i) + Q(\cos(K_{z,1}z) - \sin(K_{z,1} * z)i))i \quad (26)$$

$$\bar{u}_{z,1} = -\Big(Q\big(K_{z,1}\sin\big(K_{z,1}z\big) + K_{z,1}\cos\big(K_{z,1}z\big)i\big) - P\Big(-K_{z,1}\sin\Big(K_{z,1}(z - z_s)\Big) + K_{z,1}\cos\Big(K_{z,1}(z - z_s)\Big)i\Big)\Big) \quad (27)$$

$$\bar{u}_{x,2} = -\Big(C\big(-l_{z,2} * \sin\big(l_{z,2}z\big) + l_{z,2}\cos\big(l_{z,2}z\big)i\big) - D\Big(l_{z,2}\sin\Big(l_{z,2}(z - z_a)\Big) + l_{z,2}\cos\Big(l_{z,2}(z - z_a)\Big) * i\Big)\Big) + k_x\Big(B\Big(\cos\Big(K_{z,2}(z - z_a)\Big) - \sin\Big(K_{z,2}(z - z_a)\Big)i\Big) + A\big(\cos\big(K_{z,2}z\big) + \sin\big(K_{z,2}z\big)i\big)\Big)i \quad (28)$$

$$\bar{u}_{z,2} = \Big(A\big(-K_{z,2}\sin\big(K_{z,2}z\big) + K_{z,2}\cos\big(K_{z,2}z\big)i\big) - B\Big(K_{z,2}\sin\Big(K_{z,2}(z - z_a)\Big) + K_{z,2}\cos\Big(K_{z,2}(z - z_a)\Big)i\Big)\Big) + k_x\Big(D\Big(\cos\Big(l_{z,2}(z - z_a)\Big) - \sin\Big(l_{z,2}(z - z_a)\Big)i\Big) + C\big(\cos\big(l_{z,2}z\big) + \sin\big(l_{z,2}z\big)i\big)\Big)i \quad (29)$$

$$\bar{u}_{x,3} = Fk_x\Big(\cos\Big(K_{z,3}(z - z_a)\Big) + \sin\Big(K_{z,3}(z - z_a)\Big)i\Big)i \quad (30)$$

$$\bar{u}_{z,3} = F\left(-K_{z,3}\sin\left(K_{z,3}(z - z_a)\right) + K_{z,3}\cos\left(K_{z,3}(z - z_a)\right)i\right) \quad (31)$$

whereas the stress tensor components can be expressed as

$$T_{xz,1} = (-2)k_x\mu_1\left(Q\left(K_{z,1}\sin\left(K_{z,1}z\right) + K_{z,1}\cos\left(K_{z,1}z\right)i\right) - P\left(-K_{z,1}\sin\left(K_{z,1}(z - z_s)\right) + K_{z,1}\cos\left(K_{z,1}(z - z_s)\right)i\right)\right)i \quad (32)$$

$$T_{xz,2} = 2 * \mu_2\left(\frac{\left(D\left(l_{z,2}^2\cos\left(l_{z,2}(z - z_a)\right) - l_{z,2}^2\sin\left(l_{z,2}(z - z_a)\right)i\right) + C\left(l_{z,2}^2\cos\left(l_{z,2}z\right) + l_{z,2}^2\sin\left(l_{z,2}z\right)i\right)\right)}{2}\right.$$

$$- \frac{k_x^2\left(D\left(\cos\left(l_{z,2}(z - z_a)\right) - \sin\left(l_{z,2}(z - z_a)\right)i\right) + C\left(\cos\left(l_{z,2}z\right) + \sin\left(l_{z,2}z\right) * i\right)\right)}{2}$$

$$+ k_x\left(A\left(-K_{z,2}\sin\left(K_{z,2}z\right) + K_{z,2}\cos\left(K_{z,2}z\right)i\right)\right.$$

$$- B\left(K_{z,2}\sin\left(K_{z,2}(z - z_a)\right)\right.$$

$$\left.\left.\left. + K_{z,2}\cos\left(K_{z,2}(z - z_a)\right)i\right)\right)i\right) \quad (33)$$

$$T_{xz,3} = 2Fk_x\mu_3\left(-K_{z,3}\sin\left(K_{z,3}(z - z_a)\right) + K_{z,3}\cos\left(K_{z,3}(z - z_a)\right)i\right)i \quad (34)$$

$$T_{zz,1} = -\lambda_1\Big(\Big(P\Big(K_{z,1}^2\cos\Big(K_{z,1}(z-z_s)\Big) + K_{z,1}^2\sin\Big(K_{z,1}(z-z_s)\Big)i\Big) + Q\big(K_{z,1}^2\cos(K_{z,1}z) - K_{z,1}^2\sin(K_{z,1}z)i\big)\Big) + k_x^2\Big(P\Big(\cos\Big(K_{z,1}(z-z_s)\Big) + \sin\Big(K_{z,1}(z-z_s)\Big)i\Big) + Q\big(\cos(K_{z,1}z) - \sin(K_{z,1}z)i\big)\Big)\Big) - 2\mu_1\Big(P\Big(K_{z,1}^2\cos\Big(K_{z,1}(z-z_s)\Big) + K_{z,1}^2\sin\Big(K_{z,1}(z-z_s)\Big)i\Big) + Q\big(K_{z,1}^2\cos(K_{z,1}z) - K_{z,1}^2\sin(K_{z,1}z)i\big)\Big) \quad (35)$$

$$T_{zz,2} = -\lambda_2\Big(\Big(B\Big(K_{z,2}^2\cos\Big(K_{z,2}(z-z_a)\Big) - K_{z,2}^2\sin\Big(K_{z,2}(z-z_a)\Big)i\Big) + A\big(K_{z,2}^2\cos(K_{z,2}z) + K_{z,2}^2\sin(K_{z,2}z)i\big)\Big) + k_x^2\Big(B\Big(\cos\Big(K_{z,2}(z-z_a)\Big) - \sin\Big(K_{z,2}(z-z_a)\Big)i\Big) + A\big(\cos(K_{z,2}z) + \sin(K_{z,2}z)i\big)\Big)\Big) - 2\mu_2\Big(\Big(B\Big(K_{z,2}^2\cos\Big(K_{z,2}(z-z_a)\Big) - K_{z,2}^2\sin\Big(K_{z,2}(z-z_a)\Big)i\Big) + A\big(K_{z,2}^2\cos(K_{z,2}z) + K_{z,2}^2\sin(kz2z)i\big)\Big) - k_x\Big(C\big(-l_{z,2}\sin(l_{z,2}z) + l_{z,2}\cos(l_{z,2}z)i\big) - D\Big(l_{z,2}\sin\Big(l_{z,2}(z-z_a)\Big) + l_{z,2}\cos\Big(l_{z,2}(z-z_a)\Big)i\Big)\Big)i\Big) \quad (36)$$

$$T_{zz,3}$$

$$= -\lambda_3 \left(F \left(K_{z,3}^2 \cos\left(K_{z,3}(z - z_a) \right) + K_{z,3}^2 \sin\left(K_{z,3}(z - z_a) \right) i \right) \right.$$

$$\left. + Fk_x^2 \left(\cos\left(K_{z,3}(z - z_a) \right) + \sin\left(K_{z,3}(z - z_a) \right) i \right) \right) - 2F\mu_3 \left(K_{z,3}^2 \cos\left(K_{z,3}(z - z_a) \right) \right.$$

$$\left. + K_{z,3}^2 \sin\left(K_{z,3}(z - z_a) \right) i \right) \qquad (37)$$

APPENDIX B

THE SCANNING ACOUSTIC MICROSCOPE

B.1 Working of the Scanning Acoustic Microscope

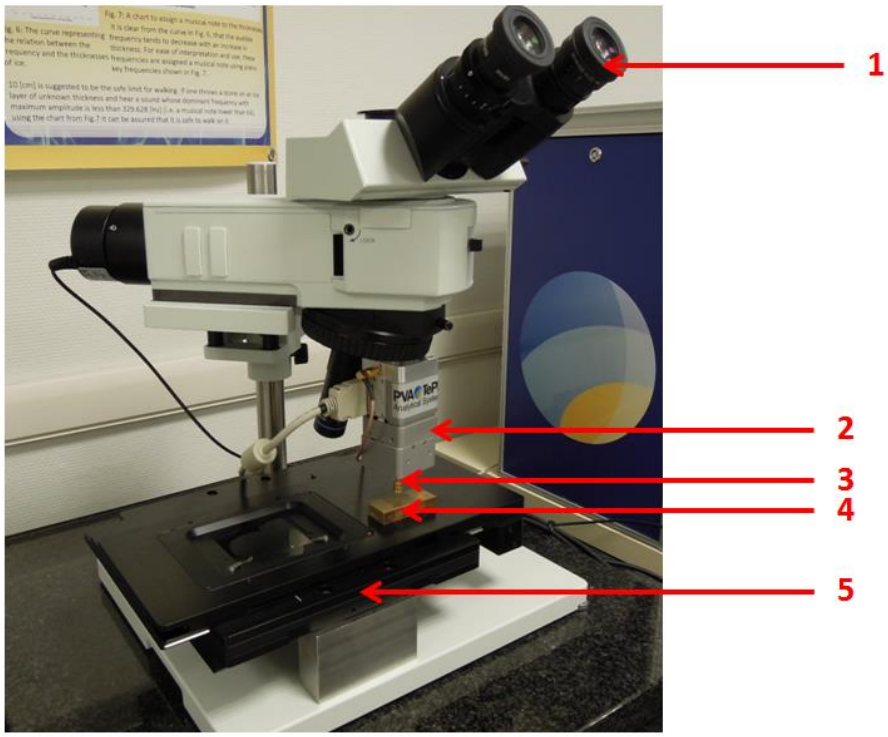

Figure 23: The scanning acoustic microscope (SAM 2000).

Table 10: The different parts of the scanning acoustic microscope.

PART NUMBER	PART
1.	Optical lens
2.	Scanner unit
3.	Transducer
4.	Sample
5.	XY Stage

The Scanning acoustic microscope (SAM 2000) manufactured by PVA TePla Analytical systems, in Figure 23 is used to test different samples. The optical lens is used to locate the desired area of the sample before performing a scan. The scanner unit is controlled by the user interface and a click wheel that can be operated manually to move in the z direction, to acquire acoustic images of the sample.

B.1.1 User interface

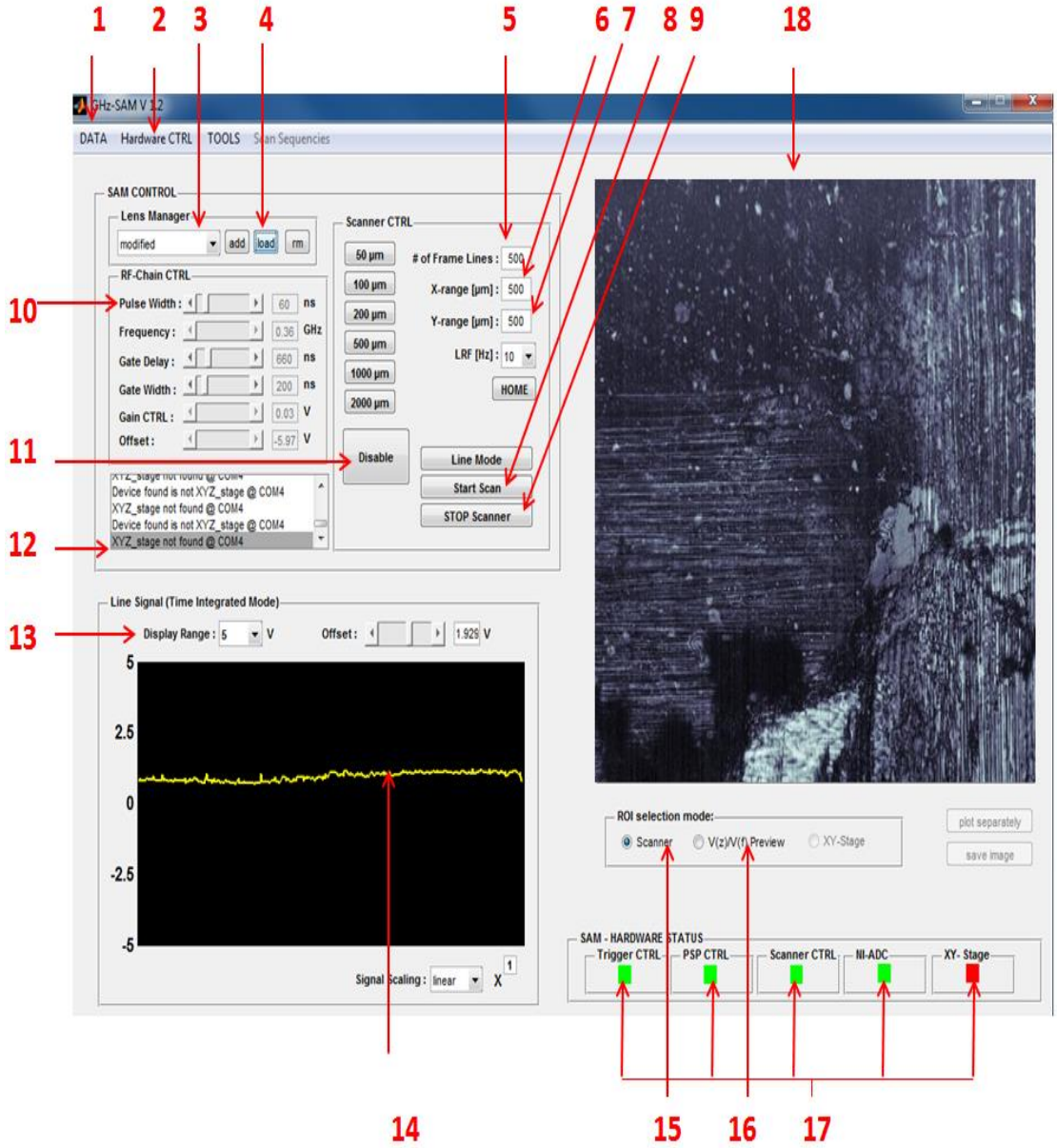

Figure 24: The user interface for the scanning acoustic microscope.

Table 11: Name and description of the different parts of the user interface.

PART NUMBER	NAME / DESCRIPTION
1.	Panel with options for data storage
2.	Panel with options for controlling the hardware units namely the XY stage, etc.
3.	"Lens Manager" / selecting lens-specific pre-defined settings
4.	Button for loading the selected lens profile
5.	Gives the scanning resolution in the x and y directions
6.	Panel for setting the scanning length in the x direction (up to 1900 μm)
7.	Panel for setting the scanning length in the y direction (up to 1900 μm)
8.	Button to start an acoustic scan of the sample
9.	Button to stop the scanner
10.	Panel for adjusting the pulse width
11.	Button to disable the transducer
12.	Communication protocol / panel showing tasks currently performed by device
13.	Panel to set the display range up to ±10 Volts
14.	Time integrated line Signal
15.	Scanner mode for acquiring individual scans
16.	V (z) curve mode for obtaining V(z) scans
17.	Status indicators for individual hardware units (on-line / off-line)
18.	Screen acoustic micrograph / acquired scan image

B.1.2 Acoustic lens

Figure 25 shows the acoustic transducers used to conduct experiments for this work. The frequencies used are 400 MHz and 1.09 GHz. Both lenses have a Sapphire body. A concave spherical surface is ground on one side of the Sapphire body. This surface provides a focusing action. A glass based matching layer at the tip of the lens optimizes the transmission of the waves. This base is fragile hence great care is taken in handling it. A transducer is placed on the side opposite to the concave surface, which when energized, generates plane waves which propagate through the lens. Generally water is used as a coupling fluid between the lens and the sample surface. These waves undergo refraction when they encounter the spherical surface of the lens. They are focused by the concave surface to a very small area called the focal area. The difference in the refractive index between the solid and the liquid improves the focusing effect even for a large numerical aperture. The clearest acoustic images are obtained when the sample is placed in the focal area. The resolution of the microscope is inversely proportional to the numerical aperture of the lens.

(a) (b)

Figure 25: (a) A focused transducer with a frequency range of 0.8 – 1.3 GHz **(b)** A 400 MHz focused transducer.

To maximize the performance of each lens, a large range of parameters; namely, beam width, excitation frequency, gate width, etc., are adjusted to develop lens profiles. The pre-designed lens profiles in the user interface, for the respective transducers, are used to acquire acoustic images.

Depending on the lens being used, the working distance, i.e. the distance between the tip of the lens and the sample surface, vary largely and can be as low as 40 μm. Since this is very small to be perceived by the naked eye, the change in the time integrated signal is relied upon for focusing. The scanner unit is lowered manually until the tip of the lens touches the coupling fluid (in this work, distilled water is used as a coupling

medium). The wheel for fine tuning is used to lower the scanner unit while the change in the time integrated signal is observed. The transducer is known to focus on the sample surface, when the time integrated signal shows the highest magnitude. The variation in amplitude may differ in magnitude for different sample and transducer frequency combinations, hence it may or may not be noticeable depending on the display range of the signal. The panel for the display is therefore, adjusted accordingly. The minimum variation in amplitude must be ±2 μm.

B.1.3 Software setting optimization

The custom made software GHz- SAM version 1.2 developed by PVA TePla Analytical systems, for Windows 7, is currently used as the control software for the scanning acoustic microscope. Individual lens profiles contain optimized settings for individual transducers, although there is room for further modification. Some parameters can still be adjusted using the panels available in the user interface to suit the requirements. Some of these parameters are described below.

1. *Excitation Frequency:* The microscope uses tone bursts to excite surface waves in the sample. The required central frequency for each lens may differ for different cases, depending on the sample under investigation. This frequency can be adjusted within the permissible bandwidth, for optimization of the image resolution.
2. *Width of Tone Burst*: The width of the transmit tone-burst can be adjusted from 10 ns to 100 ns depending upon the energy required in the signal.

3. *Gate Delay:* The gate position of the time window used for extracting the line signal can be adjusted using the gate delay panel. This delay corresponds to the time of flight of the acoustic signal, i.e. time taken to reach the focal point and return.
4. *Gate Width*: The width of the gate for the received signal can also be adjusted to obtain an improved signal depending on the different cases of application.
5. *Offset*: The offset of the line signal can be adjusted by controlling the analog pre-processing unit of the scanning acoustic microscope. Due internal reflections within the lens, while positioning the data gate for the received signal, there might be an overlap. This might cause an offset in the line signal. In order to ensure the use of the entire dynamics of the analog signal unit, the offset of the line signal should always be adjusted to zero. A change in any of these parameters affects the entire dynamics of the signal and might require refocusing of the scanner unit on the sample.

B.1.4 Image acquisition and data storage

After the settings have been optimized, and the scan area is set to the desired position, an acoustic image or in other words, an acoustic micrograph is obtained. The settings for each scan and the scan data are stored as temporary files which can be accessed using the "DATA" option in the user interface.

With the help of the scan monitor window, one can easily access the acquired image files, anytime during a session. The scan monitor window can be opened using the "Open Result Management" entry in the "DATA" menu in the user interface. The settings for and the data of a particular micrograph can be stored from the list of scans

displayed in this window. All temporarily stored data files are deleted upon closing a GHz-SAM session, i.e. closing the control software. The files saved by the user can be accessed during any session.

Data files saved in the GSI format allow for recalling the microscope's hardware settings that were applied when the data set was recorded. The "Settings Recall" option in the scan monitor window, allows the user to recall these settings for the individual hardware units except the z position of the scanner.

B.1.5 V (z) curve generation

The scanning acoustic microscope can be controlled by the user interface to perform scans at different z positions automatically. Each scan produces an acoustic image of the scanned area. The amplitude (in Volts (V)) of the received signal at a particular position (x, y) on the acoustic image is represented as a pixel. The amplitude this (x, y) position obtained from all the scans, is plotted for the respective z positions to obtain a curve called the V (z) curve. The user is required to perform at least one scan in the scanner mode before performing a V (z) scan. The V (z) mode is used to acquire acoustic images with increasing z-position values. In other words, as the transducer move towards the sample with a fixed increment in the z direction, the microscope performs a scan and produces an acoustic image of the scanned area for every z position.

The total defocus range is different for different lenses. For a 1 GHz lens with an approximate focal length of 90 μm, a defocus range of 35 μm, i.e. the starting defocused z position with the acoustical focus above the sample surface, should be sufficient. On the other hand, the focal length of a 400 MHz lens is approximately 180 μm hence a higher defocus position is required.

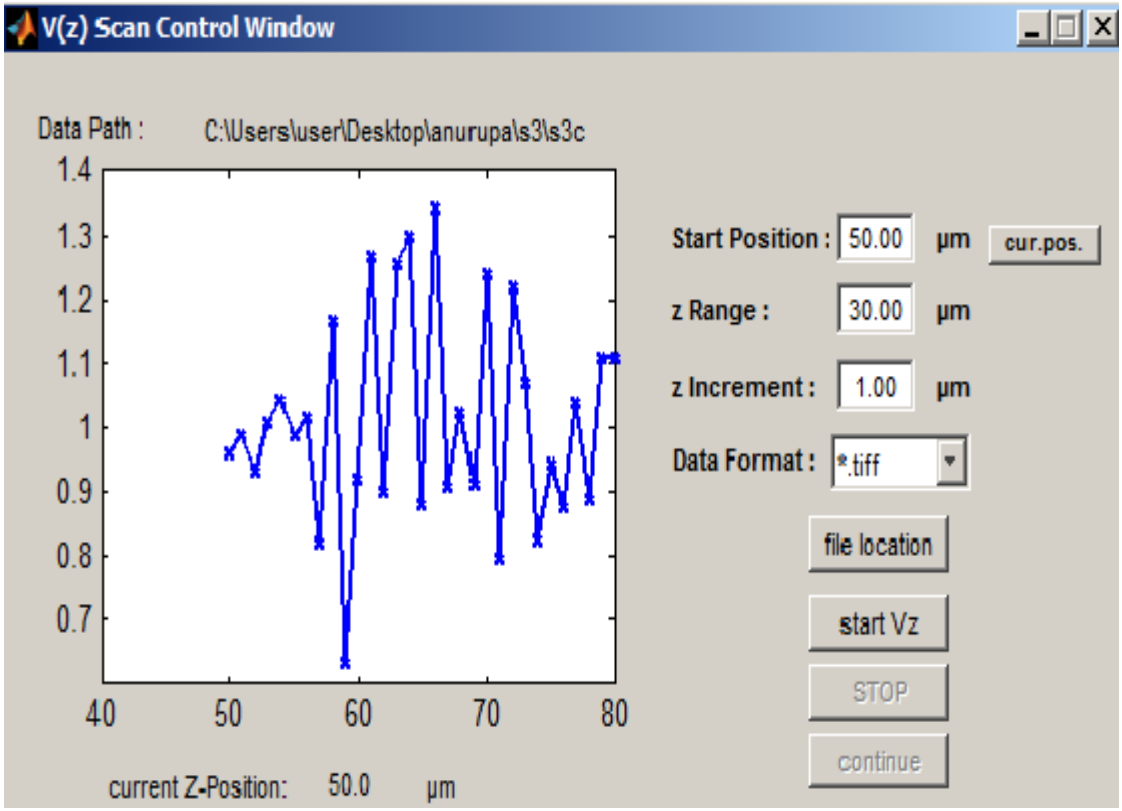

Figure 26: The settings panel for controlling the automated V (z) scan.

Figure 26 shows the control window for data acquisition in V (z) mode. This panel can be accessed from the "Scan Sequences" option in the main window of the user interface of the control software. This option is available only if at least one scan has been performed before accessing this option, during the current session. All image frames acquires during a V (z) sequence are stored as temporary files and are easily accessible from the scan monitor window.

The "start position" option shows the current position of the scanner unit in the z direction. Starting the scan from the current position avoids errors in estimation and data acquisition due to unexpected behavior of the positioning system. The "Z range" option allows the user to set the range for the V (z) scan. The maximum scan range is can be set to 35 µm. The "Z increment" option allows the user to set the spatial resolution in the z

direction. For the experiments discussed in this work, the spatial resolutions used for a 1.09 GHz lens are 0.3 μm and 0.5 μm whereas for a 400 MHz lens the resolutions used are of 1 μm and 2 μm. Once all the parameters are set, the location for saving the data is selected and the scan is conducted for the given sequence.

After the successful completion of a V (z) scan sequence, using the "continue" option, the V (z) scan can be extended to obtain the acoustic images for an extended range in the z direction. The scanner unit moves back to its start position after the completion of the V (z) scan sequence, hence the scanner unit is manually lowered to the end position of the previous scan sequence before starting the extended scan.

B.1.6 Limitations of the scanning acoustic microscope

The maximum mechanical resolution in the z direction is 0.1 μm. The maximum scan are is 1.9 x 1.9 mm. The available acoustic resolutions are 400 MHz ($\lambda \sim 3.75$ μm) and 1.09 GHz ($\lambda \sim 1.37$ μm), where λ is the wavelength. The Semi-aperture angle for both transducers ranges from 30˚to 50˚.

The system is limited to produce optical images for a depth of 210 μm for a 400 MHz transducer and 70 μm for 1.09 GHz transducer. Hence our microscope is ideal for investigating samples that are extremely thin like tissues and periodic structures of depth lower than 210 μm. Also software control for movement of the scanner unit along the z direction is possible only for a range of 30 μm at a time. Due to lack of a sample holder unit, the transducer vibration causes a drag on the sample surface during the experiment which leads to noise. This causes errors in measurements and calculation.

A lot of time has been spent in optimizing the experimental setup to reduce these effects. In the near future, time signal acquisition and an increase in the acoustic resolution to 2 GHz ($\lambda \sim 0.75\ \mu m$) will be possible.

REFERENCES

[1]. <http://www.dnr.state.mn.us/safety/ice/thickness.html> (date last viewed 24/01/2014).

[2]. Olga Chernets. "Estimation of arctic ice thickness from ambient noise." PhD thesis, Massachusetts Institute of Technology, Boston, September 1995.

[3]. James K. Lewis and Maria R. Giufrida. "Sea-Ice Kinematics as Determined by Remotely-Sensed Ice Drift: Seasonal Space and Time Scales." Photogrammetric Engineering and Remote Sensing, Vol.55, No.8, August 1989, pp. 1113-1121.

[4]. James K. Lewis, Randy D. Crissman and Warren W. Denner. "Estimating Ice Thickness and Internal Pressure and Stress Forces in Pack Ice Using Lagrangian Data." Journal of Geophysical Research, Vol.91, No. C7, July 15,1986, pp.8537-8541

[5]. Maurice Ewing, A. P. Crary and A. M. Thorne. "Propagation of Elastic Waves in Ice. Part I". Journal of Applied Physics, Vol. 5, June, 1934, pp 165- 168.

[6]. Maurice Ewing and A. P. Crary. "Propagation of Elastic Waves in Ice. Part II". Journal of Applied Physics, Vol. 5, July, 1934, pp 181- 184.

[7]. F. Press, M. Ewing, A. P. Crary, S. Katz and J. Oliver. "Air-coupled Flexural Waves in Floating Ice". Geophysical Research papers No. 6, Geophysical Research Directorate, Air Force Cambridge Research Laboratories, November 1950.

[8]. David C. Henley. "Attenuating the ice flexural wave on arctic seismic data". CREWES Research Report, Vol. 16, 2004.

[9]. Hyuck Chung and Colin Fox. "Propagation of Flexural waves at the interface between Floating plates". Proceedings of The Twelfth (2002) International Offshore and Polar Engineering Conference, Kitakyushu, Japan, May 26–31, 2002.

[10]. Bryan R. Kerman. “Sea Surface Sound: Natural Mechanisms of Surface Generated Noise in the Ocean”. Springer, Jan 1, 1988, 639 pages.

[11]. Fox, C. “Scaling laws for flexural waves in floating ice”. Proceedings of IUTAM Scaling Lows in Ice Mechanics and Ice Dynamics. Fairbanks, Alaska, USA, 2000.

[12]. Fox, C, and Squire. “On the oblique reflexion and transmission of ocean waves at shore fast sea ice”. Phil. Trans.R. Soc. Lond., Vol. 347, 1994, No A, pp 185-218.

[13]. David N. Thomas, Gerhard S. Dieckmann. “Sea Ice”.2nd edition, Wiley-Blackwell, October 2009, 640 pages.

[14]. T. C. Yang andT. W. Yates. “Flexural wave in a floating ice sheet: modeling and comparison with data”. J. Acoust. Soc. Am., Vol. 97, issue 2, 1995.

[15]. <http://www.wikihow.com/Know-When-Ice-is-Safe> (date last viewed 06/01/2013)

[16]. B. J. Mason. “T*he Physics of Clouds.”* (Clarendon Press, Oxford University Press [2nd edition], 1971), 671 pages.

[17]. Jon E. Zufelt and Robert Ettema. “Model Ice Properties”. National Technical Information Service (NTIS), Springfield, Virginia 22161. February 1996.

[18]. J.-P. Sessarego, J. Sagéloli, C. Gazanhes and H. Überall. “Two Scholte–Stoneley waves on doubly fluid-loaded plates and shells.” J. Acoust. Soc. Am. Vol. 101(1), January 1997.

[19]. Claire Prada and Mathias Fink. “Separation of interfering acoustic scattered signals using the invariants of the time-reversal operator. Application to Lamb waves characterization.” J. Acoust. Soc. Am. 104 (2), Pt. 1, August 1998.

[20]. M. Destrade. “Explicit secular equation for Scholte waves over a monoclinic crystal.” Journal of Sound and Vibration, Vol. 273, 2004, pp 409–414.

[21]. Katrien MAMPAERT. “Diffraction of ultrasonic plane waves at a periodic grating: Fundamental theory and experimental verification.” PhD thesis, Katholieke University Leuven, 1989.

[22]. I.A. Vicktorov. “Rayleigh and Lamb waves: physical theory and applications”. Plenum Press, New York, 1957,154 pages.

[23]. Achenbach, J. D. “Wave propagation in elastic solids”. North Holland, Amsterdam, 1973, 274 pages.

[24]. Achenbach J. D. “Flaw characterization by ultrasonic scattering methods”. In Solid mechanics research for quatitative non-destructive evaluation(ed J.D. Achenbach and Y. Rajapakse), Nijhoff, Dordrecht, pp.67-71.

[25]. R. Stoneley, ‘‘Elastic waves at the surface of separation of two solids’’. Proc. R. Soc. London, Ser. , 1924 A 106, 416–420.

[26]. J.-L. Izbicki, J.-L. Rousselot, A. Ge´rard, G. Maze, and J. Ripoche.‘‘Analysis of resonances related to Scholte–Stoneley waves around circular cylindrical shells,’’ J. Acoust. Soc. Am. 90, 1991, 2602–2608.

[27]. J. Dickey, G. Maidanik, and H. U ¨ berall, ‘‘The splitting of dispersion urves for the fluid loaded plate,’’ J. Acoust. Soc. Am. 98,1995, 2365–2367.

[28]. Balmforth, NJ, and Craster. “Ocean waves and ice sheets”. J. Fluid Mech., 1999, Vol 395, pp 89-124.

[29]. Crighton. “The free and forced waves on a fluid-loaded elastic plate". J. Sound Vib., DG 1979,Vol 63, pp 225-235.

[30]. Evans, DV, and Davies.”Wave-Ice Interaction Repot1313”. Davidson Laboratory, Stevens Institute of Technology, Hoboken.

[31]. Fox, C (2000). “Scaling laws for flexural waves in floating ice”. Proceedings of IUTAM Scaling Lows in Ice Mechanics and Ice Dynamics. Fairbanks, Alaska, USA.

[32]. Anurupa Shaw and Nico F.Declercq. “Ice thickness determination with audio sound”. Proceedings of Meetings on Acoustics, Vol. 19, June 2013.

[33]. Anurupa Shaw and Nico F.Declercq. “Ice thickness determination with audio sound”. (Conference presentation)J. Acoust. Soc. Am., 133, June 2013.

[34]. Anrupa Shaw, Suk Wang Yoon and Nico F. Declercq. “Investigation of sound diffraction using periodic nano-structures using acoustic microscopy”. (Conference presentation)J. Acoust. Soc. Am., 134, December 2013.

[35]. Chiaki Miyasaka, Brenard R. Tittmann and Shun- Ichiro Tanaka. “Characterization of Stress at a Ceramic/Metal Joined Interface by the V (z) Technique of Scanning Acoustic Microscopy”.Transaction of ASME, August 2002, Vol 124, pp 336-342.

[36]. Yamaoka, Yamaguchi, Sekine, Zenbutsu, Matsubara and Hayashi. “Application of Ultrasonic Microscopy to Evaluation of electrically Ligated Vessel Tissue”. Japanese of Applied Physics, July 2013, Vol 52.

[37]. Andrew Briggs and Oleg Kolosov. “Acoustic Microscopy”. Second edition, Oxford University Press Inc. New York, 2010, 345 pages.

[38]. Lemons, R. A. and Quate.”Acoustic microscope- scanning version”. Appl. Phys. Lett. 1974, pp 163-165, [18-22].

[39]. Levin, V. M., Maev, R.G. Kolosov, O.B., Senjushkina, T.A., and Bukhny, M.A. “theoretical fundamentals of quantitative acoustic microscopy”. Acta Phys. Slov. 40,1990, pp. 171-184, [109].

[40]. Roman Gr. Maev.” Acoustic Microscopy: Fundamentals and Applications”. John Wiley & Sons, Sep 2, 2008, 273 pages.

[41]. Xuegen Zhao, Riaz Akhtar, Nadja Nijenhuis, Steven J. Wilkinson, Lilli Murphy, Christoph Ballestrem, Michael. J. Sherratt, Rachel E.B. Watson, and Brian Derby. "Multi layer phase Analysis: Quantifying the elastic properties of soft tissues and live cells with Ultra high frequency scanning acoustic microscope". IEEE Trans Ultrason Ferroelectr Freq Control, April 2012, Vol. 59(4), pages 610–620.

[42]. Steve D. Sharples, All-Optical Scanning Acoustic Microscope The University of Nottingham, May 2003.

[43]. S. Ahn, J. D. Achenbach, Z. L. Li, J. O. Kim. "Numerical modeling of the V (z) curve for a thin-layer/substrate configuration". Research in Nondestructive Evaluation, 1991, Vol. 3, Issue 4, pp 183-200.

[44]. Lord Rayleigh. "Theory of sound". Dover publications, Vol 2, New York, pp. 86-96.

[45]. K. Mampaert and O. Leroy."Reflection and transmission of normally incident ultrasonic waves on periodic solid-liquid interfaces". J. Acoustic. Soc. Am. 83, 1390, 1988.

[46]. J.L. Uretskey. "The scattering of plane waves from periodic surface". Ann. Phys. 33, 400, 1965.

[47]. J. Liu and Nico F. Declercq. "Ultrasonic geometrical characterization of periodically corrugated surfaces". Ultrasonics, 53, 853-861. 2013.

[48]. S.W. herbison, J. M. Vander Weide, Nico. F. Declercq. "Observation of ultrasonic backward beam displacement in transmission through a solid having superimposed periodicity". Appl. Phys. Lett. 97, 041908, 2010.

[49]. R. Roberts, J.D. Achenbach, R. Ko, L. Alder, A. Jungman, and GQuentin. "Reflection of a beam of elastic waves by a periodic surface profile". Wave motion 7, 67 , 1985.

[50]. < http://www.pva-analyticalsystems.com/en/principle/properties> last viewed 22/01/2014.

[51]. <http://www.soest.hawaii.edu/HIGP/Faculty/zinin/Zi-subsurface.html > last viewed 22/01/2014.

[52]. <http://www.guildoptics.com/sapphires.php> last viewed 22/01/2014.